

Inflation and instabilities of a spherical magnetoelastic balloon

Shaikh Nadeem Karim^a, Ganesh Tamadapu^a

^a*Department of Applied Mechanics and Biomedical Engineering, Indian Institute of Technology
Madras, Chennai, 600036, India*

Abstract

This study explores the instabilities during the axisymmetric inflation of an initially spherical magnetoelastic balloon, modeled as a magnetizable Ogden material, under combined internal pressure and a non-uniform magnetic field generated by current-carrying coils. The nonlinear interplay of geometric and material effects leads to governing equations sensitive to bifurcations and instabilities. A coordinate singularity at the poles of the balloon is identified within the system of governing differential equations, which is resolved through an appropriate choice of field variables and L'Hôpital's rule. Stability analysis reveals that as inflation progresses, axisymmetry is broken through a supercritical pitchfork bifurcation, resulting in a pear-shaped equilibrium. This symmetry is later restored through a reverse subcritical pitchfork bifurcation, forming an isolated loop of pear-shaped solutions containing stable and unstable branches in the case of a six-parameter Ogden material model (SPOM). The onset of symmetry-breaking bifurcations is influenced by material parameters and magnetic field intensity, with critical values beyond which such bifurcations are suppressed. Both symmetry-preserving and pear-shaped configurations are stable under small asymmetric perturbations in both magnetic and non-magnetic cases. Snap-through transitions between pear-shaped and axisymmetric configurations are also observed.

Keywords: Magnetoelastic balloon, Symmetry breaking bifurcation, Snap through, Supercritical pitchfork bifurcations, Reverse subcritical pitchfork bifurcation

1. Introduction

The inflation mechanics of a polymeric membrane is a classical and intriguing problem, as it involves both material and geometric nonlinearity. Understanding the mechanics of

thin-walled structures is important in the design across scales, from nano-scale structures (Yao et al., 2011) to large-scale space structures (Jenkins, 2001). The control of pressure in inflatable structures has emerged as a trending strategy for agile and rapid actuation of soft robots (Bartlett et al., 2015). Inflatable polymer structures are also being utilized in the development of advanced surgical tools for minimally invasive procedures (Kim et al., 2011) and in bio-electronics applications (Yi et al., 2023). Many biological materials like cell membranes, tissues, arterial walls, etc. can be modeled as an inflatable polymeric membrane (Humphrey, 2003).

The inflation behavior of elastomeric and gel balloons involves both geometric and material nonlinearity, making the governing equations prone to various bifurcations. These mathematical bifurcations manifest as different physical instabilities. The inflation of thin-walled polymeric structures has been extensively studied, with a focus on explaining the instabilities that arise during the process. Among the most notable is the limit point instability, characterized by a non-monotonic relationship between pressure and stretch (Tamadapu et al., 2013).

Other prominent phenomena include wrinkling, where localized buckling occurs in the membrane due to compressive stresses, and symmetry breaking or shape bifurcations, where an inflated shape transitions into another, such as a spherical balloon becoming pear-shaped. The wrinkling of pressurized cylindrical and hemispherical balloons, using the relaxed strain energy approach, is analyzed in Patil et al. (2016). The energy-based stability criteria used to study the bifurcation from a spherical to a pear-shaped balloon is discussed in Fu and Xie (2014). Additionally, the symmetry-breaking bifurcation in toroidal membranes is explored in Roychowdhury and DasGupta (2018). Numerical methods such as finite element analysis have also been employed to investigate the inflation mechanics of ellipsoidal balloons and their post-bifurcation equilibrium curves in Wang et al. (2018).

It is intriguing to explore the effects of external fields, such as magnetic, electric, and chemical potential, on the instabilities in the inflation mechanics of thin-walled structures made of active materials like dielectrics, magneto-elastics, and gels. The influence of a direct current (DC) electric field on the inflation and shape bifurcation instabilities of spheri-

cal and cylindrical inflatable structures has been investigated in Liang and Cai (2015) and Ghosh and Basu (2021), respectively.

The inflation mechanics of a toroidal magneto-elastic membrane, subject to a non-uniform magnetic field generated by a current-carrying coil placed at the center of the undeformed membrane, is examined in Reddy and Saxena (2017). Additionally, the effect of a magnetic field produced by a dipole, located along the axis of symmetry, on the inflation and wrinkling of a circular magneto-elastic plate is studied in Barham et al. (2007) and Saxena et al. (2019).

Recently, an interesting phenomenon known as the delayed burst caused by the coupling between diffusion and deformation has been documented by Cheng et al. (2019) in spherical gel balloons made from neo-Hookean material. A similar delayed burst was also observed in torus-shaped gel balloons, as reported in Tamadapu (2022), where the study used the Gent and neo-Hookean material models and introduced a novel phenomenon termed the delayed short burst specifically for Gent materials.

Existing literature on thin-walled inflatable structures made of active materials primarily focuses on configurations such as a cylindrical membrane with a magnetic field generated by a current-carrying coil placed along the cylinder's axis (Reddy and Saxena, 2018), a magneto-elastic toroidal membrane with a current-carrying coil at its center, and a circular plate under the influence of a magnetic field created by a dipole (Barham et al., 2007; Saxena et al., 2019). However, the problem of axisymmetric inflation mechanics for initially spherical magneto-elastic balloons under the influence of a magnetic field generated by the current-carrying coil(s) appears to be unexplored in the literature.

Existing stability analyses primarily focus on the stability of spherical configurations in initially spherical polymeric balloons and the emergence of pear-shaped configurations (Chen and Healey, 1991; Fu and Xie, 2014). The existence of isola bifurcations (closed loops of non-spherical solutions) was demonstrated in Chen and Healey (1991), while a theoretical framework describing isolas, where the loop shrinks to a point termed the "isola center" as a critical parameter is approached, was presented in Dellwo et al. (1982). Isola curves have been identified experimentally and numerically in various contexts, including the buckling

of spherical elastic shells Keller and Wolfe (1965), axisymmetric buckling of hollow hemispheres Bauer et al. (1970), and the buckling of elastic arches Kerr and El-Bayoumy (1968). Symmetry-breaking bifurcations in toroidal membranes (Roychowdhury and DasGupta, 2018) and instabilities in fluid-loaded cylindrical membranes (Patil et al., 2015) have also been studied. However, the effects of magnetic fields on bifurcations and instabilities in initially spherical magnetoelastic balloons remain largely unexplored.

The literature thus seems incomplete in two significant areas: First, the axisymmetric inflation mechanics of initially spherical magneto-elastic balloons, and second, the influence of magnetic fields on the bifurcations and instabilities of these spherical magneto-elastic balloons. In this paper, we address and explore these two important questions.

This study investigates the axisymmetric inflation mechanics of an initially spherical magnetoelastic balloon subjected to a non-uniform magnetic field generated by current-carrying coil(s). A variational approach is used to derive a system of non-linear coupled ordinary differential equations that account for the Ogden strain energy density, magnetic energy for weakly magnetizable materials, and pressure work. Stability is analyzed by introducing axisymmetric and asymmetric perturbations that satisfy the geometric boundary conditions of the inflation problem, focusing on the onset of symmetry-breaking bifurcations and post-bifurcation deformations. As the balloon inflates, the symmetric solution branch undergoes spontaneous symmetry breaking at a critical pressure via a supercritical pitchfork bifurcation, resulting in shapes that retain axial symmetry but lack symmetry in the $Y^1 - Y^2$ plane. Remarkably, the axisymmetry is restored at a lower pressure through a reverse subcritical pitchfork bifurcation, forming an isolated loop of pear-shaped solutions.

2. Kinematics of axisymmetric deformation

The finite inflation of a spherical balloon made of nonlinear magneto-elastic, incompressible polymeric material is studied in this work. Let the radius of the balloon is R_0 and thickness T_0 in the undeformed configuration. The deformed configuration is assumed to be axisymmetric (about the axis Y^3 as shown in Fig. 1). A spherical coordinate system, θ , ϕ , and ζ , respectively, in the meridional, circumferential, and normal (perpendicular to

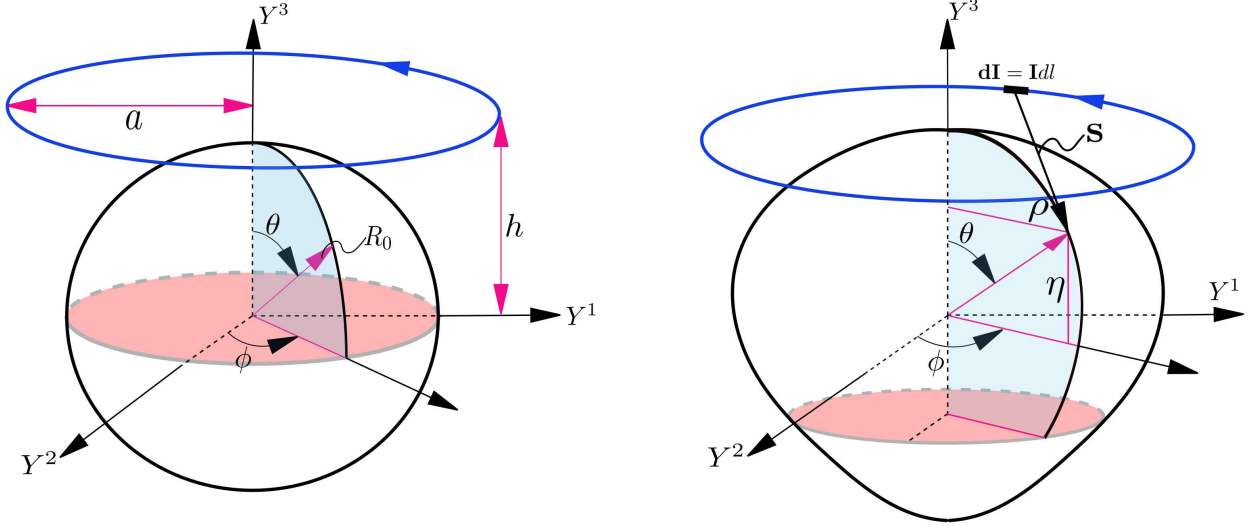


Figure 1: Undeformed and deformed configuration of initially spherical balloon undergoing axisymmetric deformation under the influence of magnetic field produced by a current carrying coil.

the surface in the thickness direction) is used to formulate the finite inflation problem. The position vector \mathbf{X} of a point on the mid-surface ($\zeta = 0$) of undeformed configuration and the position vector \mathbf{x} of the same point in deformed configuration are expressed as

$$\begin{aligned}\mathbf{X}(\theta, \phi) &= R_0 \sin \theta \cos \phi \mathbf{E}_1 + R_0 \sin \theta \sin \phi \mathbf{E}_2 + R_0 \cos \theta \mathbf{E}_3, \\ \mathbf{x}(\theta, \phi) &= \bar{\rho} \cos \phi \mathbf{e}_1 + \bar{\rho} \sin \phi \mathbf{e}_2 + \bar{\eta} \mathbf{e}_3,\end{aligned}\tag{1}$$

where \mathbf{E}_i and \mathbf{e}_i are the orthonormal bases of Euclidean coordinate systems Y^i and y^i , respectively. The deformation mapping \mathcal{X} is given as,

$$\mathbf{x}(\theta, \phi) = \mathcal{X}(\mathbf{X}(\theta, \phi)).\tag{2}$$

The bases vectors \mathbf{G}_i and \mathbf{g}_i for the undeformed and deformed mid-surface respectively, are given as,

$$\mathbf{G}_i = \frac{\partial \mathbf{X}}{\partial X^i}, \quad \mathbf{g}_i = \frac{\partial \mathbf{x}}{\partial X^i} \quad \text{where } (X^1, X^2) = (\theta, \phi).\tag{3}$$

The surface normal vector \mathbf{N} in the undeformed configuration at point \mathbf{x} and the surface normal vector \mathbf{n} in the deformed configuration at point \mathbf{x} are given, respectively, as,

$$\mathbf{N} = \frac{\mathbf{G}_1 \times \mathbf{G}_2}{|\mathbf{G}_1 \times \mathbf{G}_2|} \quad \text{and} \quad \mathbf{n} = \frac{\mathbf{g}_1 \times \mathbf{g}_2}{|\mathbf{g}_1 \times \mathbf{g}_2|}. \quad (4)$$

The vector triads $(\mathbf{G}_1, \mathbf{G}_2, \mathbf{N})$ and $(\mathbf{g}_1, \mathbf{g}_2, \mathbf{n})$ form the bases in the curvilinear coordinate system (θ, ϕ, ζ) for the undeformed and deformed configurations, respectively. The quantities $G_{ij} = \mathbf{G}_i \cdot \mathbf{G}_j$ and $g_{ij} = \mathbf{g}_i \cdot \mathbf{g}_j$ for $i, j = \{1, 2, 3\}$ represent the covariant metric tensor components for the undeformed and deformed configurations, respectively. The metric tensors \mathbf{G} (undeformed) and \mathbf{g} (deformed) are expressed as,

$$\mathbf{G} = R_0^2 \mathbf{G}_1 \otimes \mathbf{G}_1 + R_0^2 \sin^2 \theta \mathbf{G}_2 \otimes \mathbf{G}_2, \quad (5)$$

$$\mathbf{g} = (\bar{\rho}_{,\theta}^2 + \bar{\eta}_{,\theta}^2) \mathbf{g}_1 \otimes \mathbf{g}_1 + \bar{\rho}^2 \mathbf{g}_2 \otimes \mathbf{g}_2. \quad (6)$$

Here, λ_3 is the principal stretch ratio in ζ direction. The components of the inverse of the metric tensors \mathbf{G} and \mathbf{g} are given as $G_{\alpha\beta}^{-1} = G^{\alpha\beta}$, and $g_{\alpha\beta}^{-1} = g^{\alpha\beta}$, respectively. The deformation gradient tensor \mathbf{F} , which is a linear mapping between the deformed and the undeformed configurations, is given as $\mathbf{F} = \mathbf{g}_\beta \otimes \mathbf{G}^\beta$. The left Cauchy-Green tensor $\mathbf{C} = \mathbf{F}^T \mathbf{F} = g_{\alpha\beta} \mathbf{G}^\alpha \otimes \mathbf{G}^\beta = g_{\alpha\beta} G^{\alpha\gamma} \mathbf{G}_\gamma \otimes \mathbf{G}^\beta$ can be written as

$$\mathbf{C} = \frac{\bar{\rho}_{,\theta}^2 + \bar{\eta}_{,\theta}^2}{R_0^2} \mathbf{G}_1 \otimes \mathbf{G}_1 + \frac{\bar{\rho}^2}{R_0^2 \sin^2 \theta} \mathbf{G}_2 \otimes \mathbf{G}_2. \quad (7)$$

In-plane principal stretches in θ and ϕ directions are given as,

$$\lambda_\theta = \frac{\sqrt{\bar{\rho}_{,\theta}^2 + \bar{\eta}_{,\theta}^2}}{R_0}, \quad \lambda_\phi = \frac{\bar{\rho}}{R_0 \sin \theta}. \quad (8)$$

The out-of-plane stretch normal to the mid-surface is $\lambda_3 = \det(\mathbf{G}) / \det(\mathbf{g})$.

3. Total potential energy

The total energy potential for a weakly magnetizable nonlinear magneto-elastic membrane inflation (Barham et al., 2008), can be written as follows,

$$E_{\text{total}} = T_0 \int_A \Phi_e(\mathbf{C}) \, dA - T_0 \int_A \Phi_m(\mathbf{C}, \mathbf{H}) \, dA - \int_v W_p \, dv, \quad (9)$$

where T_0 is the undeformed spherical balloon thickness, A is the mid-surface area of the undeformed balloon, and v is the enclosed volume of the deformed configuration. Here, Φ_e in (9) is the elastic strain energy per unit reference volume, Φ_m is the magnetisation energy per unit reference volume, and W_p is related to the pressure energy.

In this work, the material is assumed to follow incompressible Ogden material model for the elastic part of the potential, which is given as,

$$\Phi_e = \sum_{i=1}^3 \frac{\bar{\mu}_i}{\alpha_i} (\lambda_1^{\alpha_i} + \lambda_2^{\alpha_i} + \lambda_3^{\alpha_i} - 3), \quad (10)$$

where $\bar{\mu}_i$ are the material constants and α_i are the shape parameters related to shear modulus (μ) as $2\mu = \sum_{i=1}^3 \bar{\mu}_i \alpha_i$.

The magnetic energy density used is given as,

$$\Phi_m(\mathbf{C}, \mathbf{H}) = \frac{1}{2} \mu_0 \chi \mathbf{h}_a \cdot \mathbf{h}_a, \quad (11)$$

where μ_0 is the permeability of vacuum, \mathbf{h}_a is the applied magnetic field, and χ is magnetic susceptibility per unit deformed volume. In this formulation, the self-generated magnetic field is assumed to be negligible compared to the applied magnetic field (Barham et al., 2008). The applied magnetic field \mathbf{h}_a is a nonuniform magnetic field generated by a DC current-carrying circular coil of radius \bar{a} placed at height h from equatorial plane $Y^1 - Y^2$ such that the coil axis coincides with the axis of symmetry of deformation i.e. axis Y^3 . The applied field \mathbf{h}_a is derived using Biot-Saverts's law as follows,

$$d\mathbf{h}_a = \frac{I}{4\pi} \frac{d\mathbf{l} \times \mathbf{s}}{|\mathbf{s}|^3}, \quad (12)$$

where I is current in the coil, $d\mathbf{l}$ is a differential length element on the wire at an angle ϕ_i from Y^1 axis, \mathbf{s} is the position vector of a point on the mid-surface of the balloon from $d\mathbf{l}$ as shown in Fig. 1. Vectors \mathbf{s} and $d\mathbf{l}$ are obtained as follows,

$$d\mathbf{l} = -dl \sin \phi_i \mathbf{e}_1 + dl \cos \phi_i \mathbf{e}_2, \quad dl = \bar{a} d\phi_i, \quad (13)$$

$$\mathbf{s} = (\bar{\rho} \cos \phi - \bar{a} \cos \phi_i) \mathbf{e}_1 + (\bar{\rho} \sin \phi - \bar{a} \sin \phi_i) \mathbf{e}_2 + (\bar{\eta} - \bar{h}) \mathbf{e}_3, \quad (14)$$

$$d\mathbf{l} \times \mathbf{s} = d\phi_i [(\bar{\eta} - \bar{h}) \bar{a} \cos \phi_i \mathbf{e}_1 + (\bar{\eta} - \bar{h}) \bar{a} \sin \phi_i \mathbf{e}_2 + (\bar{a}^2 - \bar{\rho}\bar{a} \cos(\phi_i - \phi)) \mathbf{e}_3]. \quad (15)$$

From (12), (14) and (15), the applied magnetic field \mathbf{h}_a can be written as,

$$\mathbf{h}_a = \frac{I}{4\pi} \int_0^{2\pi} \frac{((\bar{\eta} - \bar{h}) \bar{a} \cos \phi_i) \mathbf{e}_1 + ((\bar{\eta} - \bar{h}) \bar{a} \sin \phi_i) \mathbf{e}_2 + (\bar{a}^2 - \bar{\rho}\bar{a} \cos(\phi_i - \phi)) \mathbf{e}_3}{\left(\bar{\rho}^2 + (\bar{\eta} - \bar{h})^2 + \bar{a}^2 - 2\bar{\rho}\bar{a} \cos(\phi_i - \phi)\right)^{3/2}} d\phi_i. \quad (16)$$

Introducing the non-dimensional quantities $(\rho, \eta, a, h) = (\bar{\rho}, \bar{\eta}, \bar{a}, \bar{h}) / R_0$, the applied magnetic field \mathbf{h}_a can be rewritten as,

$$\mathbf{h}_a = \frac{I}{4\pi R_0} \int_0^{2\pi} \frac{((\eta - h) a \cos \phi_i) \mathbf{e}_1 + ((\eta - h) a \sin \phi_i) \mathbf{e}_2 + (a^2 - \rho a \cos(\phi_i - \phi)) \mathbf{e}_3}{\left(\rho^2 + (\eta - h)^2 + a^2 - 2\rho a \cos(\phi_i - \phi)\right)^{3/2}} d\phi_i. \quad (17)$$

The magnetic energy Φ_m can be written as,

$$\Phi_m = \frac{1}{2} \mu_0 \chi \mu \mathcal{M} \mathcal{H}^2, \quad (18)$$

where $\mathcal{M} = I^2 / 16\pi^2 R_0^2 \mu$ and

$$\mathcal{H} = \left| \int_0^{2\pi} \frac{((\eta - h) a \cos \phi_i) \mathbf{e}_1 + ((\eta - h) a \sin \phi_i) \mathbf{e}_2 + (a^2 - \rho a \cos(\phi_i - \phi)) \mathbf{e}_3}{\left(\rho^2 + (\eta - h)^2 + a^2 - 2\rho a \cos(\phi_i - \phi)\right)^{3/2}} d\phi_i \right| \quad (19)$$

The third term in (9) represents the internal energy due to the presence of gas at gauge pressure \bar{P} , where the integral is performed over the deformed/inflated volume, and expressed as

$$\int_v W_p dv = \int_0^{2\pi} \int_0^\pi \left(\frac{1}{3} P \mathbf{x} \cdot \mathbf{n} \sqrt{g} \right) d\theta d\phi = - \int_0^{2\pi} \int_0^\pi \left(\frac{1}{2} P \rho^2 \eta_{,\theta} \right) d\theta d\phi \quad (20)$$

where \mathbf{x} is the position vector given in (1) and $g = \det(\mathbf{g})$ is the determinant of the deformed metric tensor.

4. Governing equations

The total potential energy \bar{E}_T for axisymmetric inflation of a magneto-elastic polymeric balloon can be written as,

$$\bar{E}_T = \int_0^{2\pi} \int_0^\pi \left[(\Phi_e - \Phi_m) T_0 \sqrt{G} + \frac{1}{2} \bar{P} \bar{\rho}^2 \bar{\eta}_{,\theta} \right] d\theta d\phi, \quad (21)$$

where $G = \det(\mathbf{G})$ is the determinant of the undeformed metric tensor. Substituting Φ_m from (11) in 21,

$$\bar{E}_T = \int_0^{2\pi} \int_0^\pi \left[\left(\Phi_e - \frac{1}{2} \mu_0 \chi \mu \mathcal{M} \mathcal{H}^2 \right) T_0 R_0^2 \sin \theta + \frac{1}{2} \bar{P} \bar{\rho}^2 \bar{\eta}_{,\theta} \right] d\theta d\phi, \quad (22)$$

\bar{E}_T is a functional in terms of primary field variables and independent variable θ i.e. $\bar{E}_T = \bar{E}_T(\bar{\rho}, \bar{\rho}_{,\theta}, \bar{\eta}, \bar{\eta}_{,\theta}, \theta)$. A primary field variable $\bar{\rho}$ is replaced with λ_2 as the new primary field variable by doing the following substitutions,

$$\bar{\rho} = \lambda_2 R_0 \sin \theta, \quad \lambda_{2,\theta} \sin \theta = v, \quad \bar{w} = \bar{\eta}_{,\theta}, \quad \lambda_1 = \frac{\sqrt{(\lambda_2 \cos \theta + v)^2 R_0^2 + \bar{w}^2}}{R_0}, \quad (23)$$

The total potential energy is non-dimensionalized using $\mu^* = \mu/2$,

$$(\rho, \eta, w, a) = \frac{(\bar{\rho}, \bar{\eta}, \bar{w}, \bar{a})}{R_0} \quad \hat{\Phi} = \frac{\Phi_e}{\mu^*} \quad P = \frac{\bar{P} R_0}{T_0 \mu^*}, \quad E_T = \frac{\bar{E}_T}{\mu^*}, \quad \mu_i = \frac{\bar{\mu}_i}{\mu^*}, \quad (24)$$

where $\bar{\mu}_i$ and μ_i are dimensional and non-dimensionalised material parameters for Ogden material model given in (10).

Using equations (24) and (23) total potential energy can be written as,

$$E_T = \int_0^{2\pi} \int_0^\pi \left[\left(\hat{\Phi} - \frac{1}{2} \mu_0 \chi \mathcal{M} \mathcal{H}^2 \right) \sin \theta + \frac{1}{2} P \lambda_2^2 \eta_{,\theta} \sin^2 \theta \right] d\theta d\phi, \quad (25)$$

$$E_T = \int_0^{2\pi} \int_0^\pi \hat{\Pi} d\theta d\phi,$$

Total potential energy functional now becomes $E_T = E_T(\lambda_2, v, \eta, w, \theta)$. Using the principle of minimum potential energy, equations of equilibrium are obtained as

$$\frac{\partial \hat{\Pi}}{\partial \lambda_2} - \frac{d}{d\theta} \left(\frac{\partial \hat{\Pi}}{\partial v} \sin \theta \right) = 0, \quad \frac{\partial \hat{\Pi}}{\partial \eta} - \frac{d}{d\theta} \frac{\partial \hat{\Pi}}{\partial w} = 0. \quad (26)$$

The boundary conditions for axisymmetric inflation of the balloon are given as

$$\rho(0) = 0, \quad \rho(\pi) = 0, \quad \eta_{,\theta}(0) = 0, \quad \eta_{,\theta}(\pi) = 0. \quad (27)$$

Substituting (23) in (26) converts a set of two second-order ordinary differential equations (26) to a set of four first-order ordinary differential equations given as

$$\lambda_{2,\theta} = \frac{v}{\sin \theta}, \quad (28)$$

$$v_{,\theta} = F_1(v, \eta, w, \lambda_2, \theta; P), \quad (29)$$

$$w_{,\theta} = F_2(v, \eta, w, \lambda_2, \theta; P), \quad (30)$$

$$\eta_{,\theta} = w \quad (31)$$

with the boundary conditions in terms of new field variables as,

$$v(0) = 0, \quad w(0) = 0, \quad v(\pi) = 0, \quad w(\pi) = 0. \quad (32)$$

Due to the coordinate singularity at the poles ($\theta = 0$ and $\theta = \pi$), the right hand side of the equations (28) -(31) attain an indeterminate $0/0$ form and are thus valid only for $\theta \neq 0$ and $\theta \neq \pi$. Applying L'Hospital's rule to indeterminate form, set equations valid for the poles are given as, $\lambda_{2,\theta} = 0$, $v_{,\theta} = 0$, $w_{,\theta} = (-\mu_o \chi \mathcal{M} \mathcal{H} \mathcal{H}_{,\eta} - P \lambda_2^2 \cos \theta) / (2\Phi_{,ww})$, $\eta_{,\theta} = 0$. (see Appendix A.1 for details)

5. Solution procedure

Following a similar procedure used in Roychowdhury and DasGupta (2015a,b); Tamadapu (2022); Tamadapu and DasGupta (2014a) and Tamadapu and DasGupta (2014b), the two-point boundary value problem (TPBVP) given by (28)-(32) for the axisymmetric inflation of a magneto-elastic balloon is solved as follows. For the plane of symmetric solutions one would expect the stretches at the poles should be same. First, λ_2 value at $\theta = 0$ is chosen for a fixed value of \mathcal{M} with pressure P and $\eta(0)(= \eta(\pi))$ as unknown quantities to be determined using shooting method. The ode set (28) is integrated from $\theta = 0$ to $\pi/2$ and $\theta = \pi$ to $\pi/2$ with P and $\eta(0) = \eta(\pi)$ as guess values. The correct values of pressure and η at the poles are obtained by shooting method with a cost function from the matching conditions at $\theta = \pi/2$ as given below:

$$S(P, \eta(0), \lambda_2(\pi), \eta(\pi); \lambda_2(0)) = \left[\{\lambda_2^f(\pi/2) - \lambda_2^b(\pi/2)\}^2 + \{v^f(\pi/2) - v^b(\pi/2)\}^2 + \{w^f(\pi/2) - w^b(\pi/2)\}^2 + \{\eta^f(\pi/2) - \eta^b(\pi/2)\}^2 \right]^{1/2}.$$

Here, superscripts f and b represent the forward ($\theta = 0$ to $\pi/2$) and backward ($\theta = \pi$ to $\pi/2$) integration solutions, respectively. The shooting method involves searching for local minima of the cost function that satisfy $|S| < 10^{-8}$ for input values of $\lambda_2(0)$ and \mathcal{M} , which yields an exact solution for the 4-tuple parameter $[P, \eta(0), \lambda_2(\pi), \eta(\pi)]$. The shooting method is implemented through the Nelder–Mead search technique (Nelder and Mead (1965)) using the MATLAB `fminsearch` function.

Now the stretch value $\lambda_2(0)$ from the correct 4-tuple $[P, \eta(0), \lambda_2(\pi), \eta(\pi)]$ is given a small increment δ . For this new value of stretch $\lambda_2(0) + \delta$ at the pole, shooting method is implemented again to get the next correct 4-tuple.

6. Cauchy stresses

Following the work of Barham et al. (2008), the Cauchy stresses for the incompressible magneto-elastic material are given as follows:

$$\sigma = \frac{\partial \Phi_e}{\partial \mathbf{F}} \mathbf{F}^T + \frac{\partial}{\partial \mathbf{F}} \left(\frac{1}{2} \chi \mu_0 |\mathbf{h}_a|^2 \right) \mathbf{F}^T + \mu_0 \left(\mathbf{h}_a \otimes \mathbf{h}_a - \frac{1}{2} |\mathbf{h}_a|^2 \mathbf{I} \right) + \mu_0 \mathbf{h}_a \otimes \mathbf{m} - q \mathbf{I}, \quad (33)$$

where, $(\cdot)_{\mathbf{F}} = \frac{\partial(\cdot)}{\partial \mathbf{F}}$ denotes the partial derivative with respect to the deformation gradient \mathbf{F} , and q is the constraint pressure, serving as a Lagrange multiplier for the constrained minimization of the total energy potential E_T .

$$\left(\frac{\partial \Phi_e}{\partial \mathbf{F}} \mathbf{F}^T \right)_{\theta} = \lambda_1 \frac{\partial \Phi_e}{\partial \lambda_1}, \quad \left(\frac{\partial \Phi_e}{\partial \mathbf{F}} \mathbf{F}^T \right)_{\phi} = \lambda_2 \frac{\partial \Phi_e}{\partial \lambda_2}, \quad \left(\frac{\partial \Phi_e}{\partial \mathbf{F}} \mathbf{F}^T \right)_{\zeta} = \lambda_3 \frac{\partial \Phi_e}{\partial \lambda_3}. \quad (34)$$

$$\begin{aligned} \left[\frac{\partial}{\partial \mathbf{F}} \left(\frac{1}{2} \chi \mu_0 |\mathbf{h}_a|^2 \right) \mathbf{F}^T \right]_{\theta} &= \frac{1}{2} \chi \mu_0 \frac{\partial}{\partial \lambda_1} (|\mathbf{h}_a|^2) \lambda_1 = 0 \\ \left[\frac{\partial}{\partial \mathbf{F}} \left(\frac{1}{2} \chi \mu_0 |\mathbf{h}_a|^2 \right) \mathbf{F}^T \right]_{\phi} &= \frac{1}{2} \chi \mu \mathcal{M} \frac{\partial}{\partial \lambda_2} (\mathcal{H}^2) \lambda_2 \end{aligned}$$

The dimensional stress components are given by

$$\begin{aligned}\bar{\sigma}_\theta &= \left(\lambda_1 \frac{\partial \Phi_e}{\partial \lambda_1} - (q\mathbf{I})_\theta \right) + (1 + \chi)\mu\mathcal{M}(h_a)_\theta^2 - \frac{1}{2}\mu\mathcal{M}\mathcal{H}^2 \\ \bar{\sigma}_\phi &= \left(\lambda_2 \frac{\partial \Phi_e}{\partial \lambda_2} - (q\mathbf{I})_\phi \right) + \frac{1}{2}\lambda_2\chi\mu\mathcal{M}\frac{\partial}{\partial \lambda_2}(\mathcal{H}^2) - \frac{1}{2}\mu\mathcal{M}\mathcal{H}^2 \\ \bar{\sigma}_\zeta &= \left(\lambda_3 \frac{\partial \Phi_e}{\partial \lambda_3} - (q\mathbf{I})_\zeta \right) + (1 + \chi)\mu\mathcal{M}(h_a)_\zeta^2 - \frac{1}{2}\mu\mathcal{M}\mathcal{H}^2\end{aligned}$$

Constraint pressure q is calculated by setting the mechanical part of the stress in the thickness direction σ_ζ to zero and is given by $q = \lambda_3 \frac{\partial \Phi_e}{\partial \lambda_3}$. The expressions for the dimension less stress components (with shear modulus μ) are given by

$$\sigma_\theta = \left(\lambda_1 \frac{\partial \Phi}{\partial \lambda_1} - \lambda_3 \frac{\partial \Phi}{\partial \lambda_3} \right) + (1 + \chi)\mathcal{M}(h_a)_\theta^2 - \frac{1}{2}\mathcal{M}\mathcal{H}^2, \quad (35)$$

$$\sigma_\phi = \left(\lambda_2 \frac{\partial \Phi}{\partial \lambda_2} - \lambda_3 \frac{\partial \Phi}{\partial \lambda_3} \right) + \frac{1}{2}\lambda_2\chi\mathcal{M}\frac{\partial}{\partial \lambda_2}(\mathcal{H}^2) - \frac{1}{2}\mathcal{M}\mathcal{H}^2. \quad (36)$$

7. Stability analysis

7.1. Kinematics of asymmetric deformation

Assuming general asymmetric deformation, the deformed position vector can be written as,

$$\mathbf{x}(\theta, \phi) = \bar{\rho}(\theta, \phi) \cos[\beta(\theta, \phi)] \mathbf{e}_1 + \bar{\rho}(\theta, \phi) \sin[\beta(\theta, \phi)] \mathbf{e}_2 + \bar{\eta}(\theta, \phi) \mathbf{e}_3. \quad (37)$$

The covariant metric tensor associated with asymmetrically deformed configuration is given as,

$$\begin{aligned}\mathbf{g}_{\text{asm}} &= (\bar{\rho}^2\beta_{,\theta}^2 + \bar{\eta}_{,\theta}^2 + \bar{\rho}_{,\theta}^2) \mathbf{g}_1 \otimes \mathbf{g}_1 + (\bar{\rho}^2\beta_{,\theta}\beta_{,\phi} + \bar{\eta}_{,\theta}\bar{\eta}_{,\phi} + \bar{\rho}_{,\theta}\bar{\rho}_{,\phi}) \mathbf{g}_1 \otimes \mathbf{g}_2 \\ &+ (\bar{\rho}^2\beta_{,\theta}\beta_{,\phi} + \bar{\eta}_{,\theta}\bar{\eta}_{,\phi} + \bar{\rho}_{,\theta}\bar{\rho}_{,\phi}) \mathbf{g}_2 \otimes \mathbf{g}_1 + (\bar{\rho}^2\beta_{,\phi}^2 + \bar{\eta}_{,\phi}^2 + \bar{\rho}_{,\phi}^2) \mathbf{g}_2 \otimes \mathbf{g}_2.\end{aligned} \quad (38)$$

The principal stretches Λ_1, Λ_2 for asymmetric deformation are eigenvalues of $\mathbf{C} = \mathbf{G}^{-1}\mathbf{g}$. The out-of-plane stretch normal to the mid-surface Λ_3 is given as, $\Lambda_3 = \det(\mathbf{G})/\det(\mathbf{g}_{\text{asm}})$.

The stability of the axisymmetric solution of the governing equations given by (28)-(31) is analyzed by introducing both axisymmetric as well as asymmetric perturbations. The

primary field variables λ_2 and η which locate a material point in the deformed configuration are added with perturbation as,

$$\lambda_2^*(\theta, \phi) = \lambda_2^{(0)}(\theta) + \epsilon \lambda_2^{(1)}(\theta) + \epsilon \lambda_2^{(2)}(\theta) \cos \phi + \mathcal{O}(\epsilon^2), \quad (39)$$

$$\eta^*(\theta, \phi) = \eta^{(0)}(\theta) + \epsilon \eta^{(1)}(\theta) + \epsilon \eta^{(2)}(\theta) \cos \phi + \mathcal{O}(\epsilon^2), \quad (40)$$

$$\beta^*(\theta, \phi) = \theta + \epsilon \beta^{(2)}(\theta) \sin \phi + \mathcal{O}(\epsilon^2), \quad (41)$$

where ϵ is a book-keeping parameter for the perturbation, λ_2^*, η^* and β^* are perturbed primary field variables, $\lambda_2^{(0)}$ and $\eta^{(0)}$ are solutions of the axisymmetric inflation problem, $\lambda_2^{(1)}, \eta^{(1)}$, are introduced perturbations to study the plane of symmetry breaking solution, $\lambda_2^{(2)}, \eta^{(2)}$ and $\beta^{(2)}$ are introduced perturbations to study asymmetric solution. The membrane is perturbed from the axisymmetric solution to the plane of symmetry breaking or complete asymmetric solution to study the linear stability problem and to find the possible existence of the plane of symmetry breaking or asymmetric solution branch.

The perturbations introduced for the primary field variables are given in terms of Legendre's polynomial functions are given as,

$$\lambda_2^{(i)}(\theta) = \sum_{k=1}^N a^{i,k} P_k(\cos \theta), \quad \eta^{(i)}(\theta) = \sum_{k=1}^N b^{i,k} P_k(\cos \theta), \quad \beta^{(2)}(\theta) = \sum_{k=1}^N c^{2,k} P_k^1(\cos \theta), \quad i = 1, 2. \quad (42)$$

Using (39)-(42) perturbed left Cauchy-Green tensor \tilde{C} and the perturbed total energy potential E_T^* are calculated. The perturbed total energy potential E_T^* is expressed as,

$$E_T^* = E_T^*(\lambda_2^*, \eta^*, \beta^*). \quad (43)$$

Note that ϕ dependent perturbations are absent in the above equations for the plane of symmetry breaking solutions. In general, the perturbed total energy potential is expanded in terms of ϵ about the axisymmetric equilibrium solution up to second order in ϵ as,

$$\begin{aligned} E_T^*(\lambda_2^*, \eta^*, \beta^*) &= E_T^*(\lambda_2^{(0)}, \eta^{(0)}) + \epsilon \delta E_T^*(\lambda_2^{(0)}, \eta^{(0)}) + \epsilon^2 \delta^2 E_T^*(\lambda_2^{(0)}, \eta^{(0)}) + \mathcal{O}(\epsilon^3) \\ &= E_{T_0}^* + \epsilon E_{T_1}^* + \epsilon^2 E_{T_2}^* + \mathcal{O}(\epsilon^3) \end{aligned} \quad (44)$$

The governing equations (28)-(31) for the axisymmetric deformation are derived using the principle of minimum potential, hence the first variation of total energy potential is zero ($E_{T_1}^* = 0$). The stability of the perturbed configuration is determined by the positive definiteness of the second variation of total energy potential ($E_{T_2}^*$). The perturbed total energy potential can be written in terms of coefficients of Legendre polynomials (see equation (42)) as,

$$E_T^* = E_T^*(z^{i,1}, z^{i,2}, \dots), \quad z^i = \{a^{i,k}, b^{i,2}, c^{2,k}\}, \quad k = 1, 2, 3, \dots, N, \quad (45)$$

where $i = 1$ and $i = 2$ correspond to plane of symmetry breaking and asymmetric perturbations, respectively. The positive definiteness of the second variation $E_{T_2}^*$ is given by the Legendre-Hadamard or ellipticity condition Truesdell et al. (2004),

$$\sum_{p=1}^{(i+1)N} \sum_{q=1}^{(i+1)N} \frac{\partial^2 E_T^*}{\partial z^{i,p} \partial z^{i,q}} \Big|_{z^i=0} \delta z^{i,p} \delta z^{i,q} > 0, \quad i = 1 \text{ or } 2. \quad (46)$$

The violation of the Legendre-Hadamard condition for a chosen axisymmetric deformed configuration indicates a possible instability. This implies the second order partial derivative term (usually called as Hessian matrix) in (46) needs to be positive definite. Therefore, loosely speaking all the eigenvalues of the Hessian matrix need to be positive for the stability of a given equilibrium configuration around which perturbation are carried. At least one negative eigenvalue indicates the existence of the symmetry-breaking solutions.

8. Results and discussions

Calculations are performed for the dimensionless material parameters given in Tab. 1. The parameters μ_i and α_i are chosen such that $\sum_{i=1}^3 \mu_i \alpha_i = 4$.

8.1. Deformation in the absence of magnetic field

Consider the case with zero applied magnetic field ($\mathcal{M} = 0$). The spherical elastomeric balloon is inflated by controlling the pressure inside the balloon. The inflated configuration remains spherical until the deformation reaches a stretch value where, a bifurcation point

Ogden model	α_1	α_2	α_3	μ_1	μ_2	μ_3
SPOM1	1.3	4	-2	3.00508	0.0145	-0.0177
SPOM2	1.73	4	-2	2.25815	0.0145	-0.0177
FPOM1	1.3	0	-2	3.04969	0	-0.0177
FPOM2	1.73	0	-2	2.29168	0	-0.0177
TPOM1	1.3	0	0	3.07692	0	0
TPOM2	1.98	0	0	2.0202	0	0

Table 1: SPOM - Six parameter Ogden material, FPOM - Four parameter Ogden material, TPOM - Two parameter Ogden material.

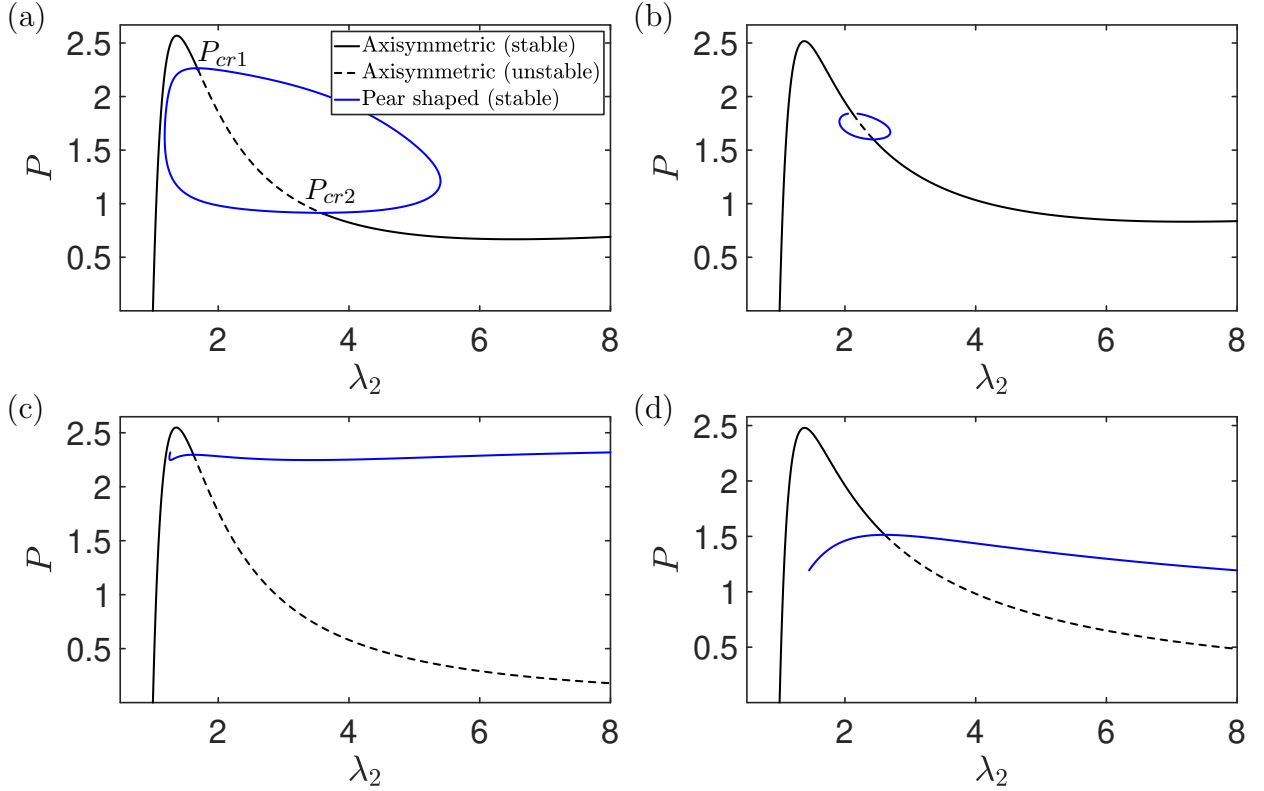


Figure 2: P vs λ_2 at the pole ($\theta = 0, \pi$) for the axisymmetric and pear-shaped deformations of the balloon in the absence of magnetic field. (a) SPOM1 and (b) SPOM2 material parameters with isola bifurcations where axisymmetric shape retains its stability after some stretch by reverse supercritical pitchfork bifurcation (c) TPOM1 and (d) TPOM2 with no isola bifurcation.

is observed beyond the limit point pressure stretch. The solutions observed after the bifurcation point are plane of symmetry breaking also called in the literature as pear-shaped configurations. Such pear-shaped solutions on either side of the axisymmetric curves represent stretches at the north and south poles and vice versa. While the bifurcation of the spherical equilibrium into a pear-shaped equilibrium is studied in Fu and Xie (2014) and Chen and Healey (1991), it is important to revisit the specific impact of material parameters on the post-bifurcation solutions, particularly in the context of Ogden type material model.

Fig. 2 demonstrates the effect of material parameters on the post-bifurcation (pear-shaped) equilibrium curve with the Ogden material model. For both SPOM and FPOM parameters (see Tab. 1), an isola bifurcation exists in the form of an isolated closed loop representing pear-shaped solutions as shown in Figs. 2(a) and 2(b). The local bifurcations show supercritical and reverse supercritical pitchfork normal behavior at the top (P_{cr1}) and bottom (P_{cr2}) bifurcation points, respectively. As α_1 increases, the isola solution curve shrinks to the isola center and eventually disappears beyond a specific critical value of α_1 . On the other hand, for TPOM parameters, there is no isola bifurcation observed (see Figs. 2(c) and 2(d)). However, supercritical pitchfork bifurcation is observed with hardening and softening type nonlinearity as shown in Figs. 2(c) and 2(d), respectively. Also, the pressure at which the plane of symmetry breaking bifurcation occurs decreases with increasing α_1 .

There is a critical value of α_1 (not shown in figures) for the SPOM, FPOM, and TPOM models beyond which pear-shaped solutions no longer exist. For the values of α_1 beyond this threshold, the spherical equilibrium remains stable, and the system does not transition to a non-spherical configuration.

8.2. Effect of magnetic field on balloon inflation: single coil arrangement

This section explores the effects of non-uniform applied magnetic field created by a current-carrying coil on the deformation mechanics of an incompressible magnetoelastic balloon. At smaller stretches, the influence of the magnetic field is negligible but becomes increasingly pronounced as the stretches grow larger. This occurs because the magnetic

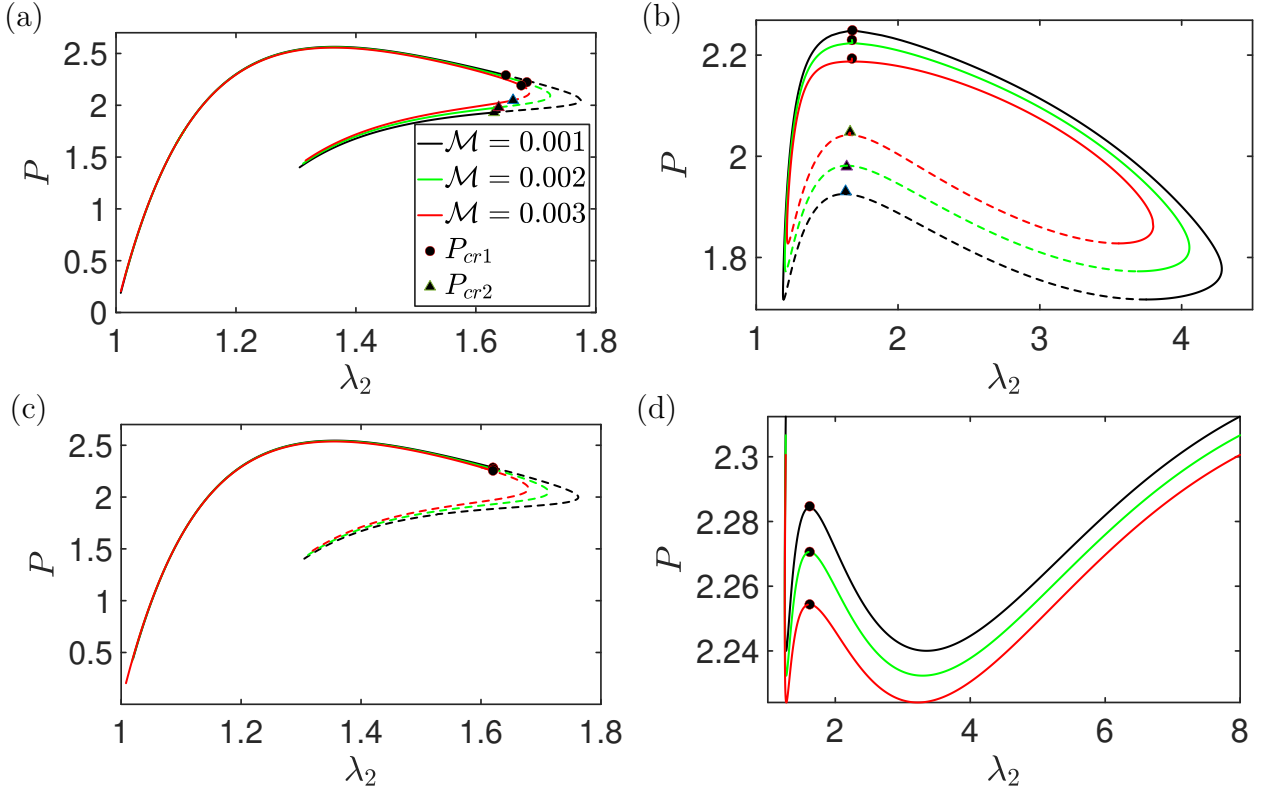


Figure 3: P vs λ_2 at pole $\theta = 0$ (a) SPOM1 plane of symmetry curve. (b) SPOM1 pear-shaped curve (c) TPOM1 plane of symmetry curve. (d) TPOM1 pear-shaped curve. The solid line represents a stable equilibrium and the dotted line represents unstable equilibrium.

field intensity diminishes as the distance between the wire and the membrane increases. A similar observation is reported in Reddy and Saxena (2017) for a toroidal membrane.

As the applied magnetic field intensity increases, the limit point pressure of the primary (plane of symmetry) curve decreases. Notably, at smaller stretch ratios, the primary curve does not have an equilibrium state at a pressure lower than a certain critical value on the left of the limit point on the primary curve. The smallest pressure in the pre-limit point region of the primary curve is commonly referred in the literature as “magnetic limit point.” At larger stretches, the primary curve exhibits a “turning point” after the limit point pressure, and this turning point occurs at progressively smaller stretches with increasing magnetic field intensity as shown in Fig. 3(a). For SPOM and FPOM parameters, another interesting feature observed with the introduction of magnetic field is the existence of multiple plane of

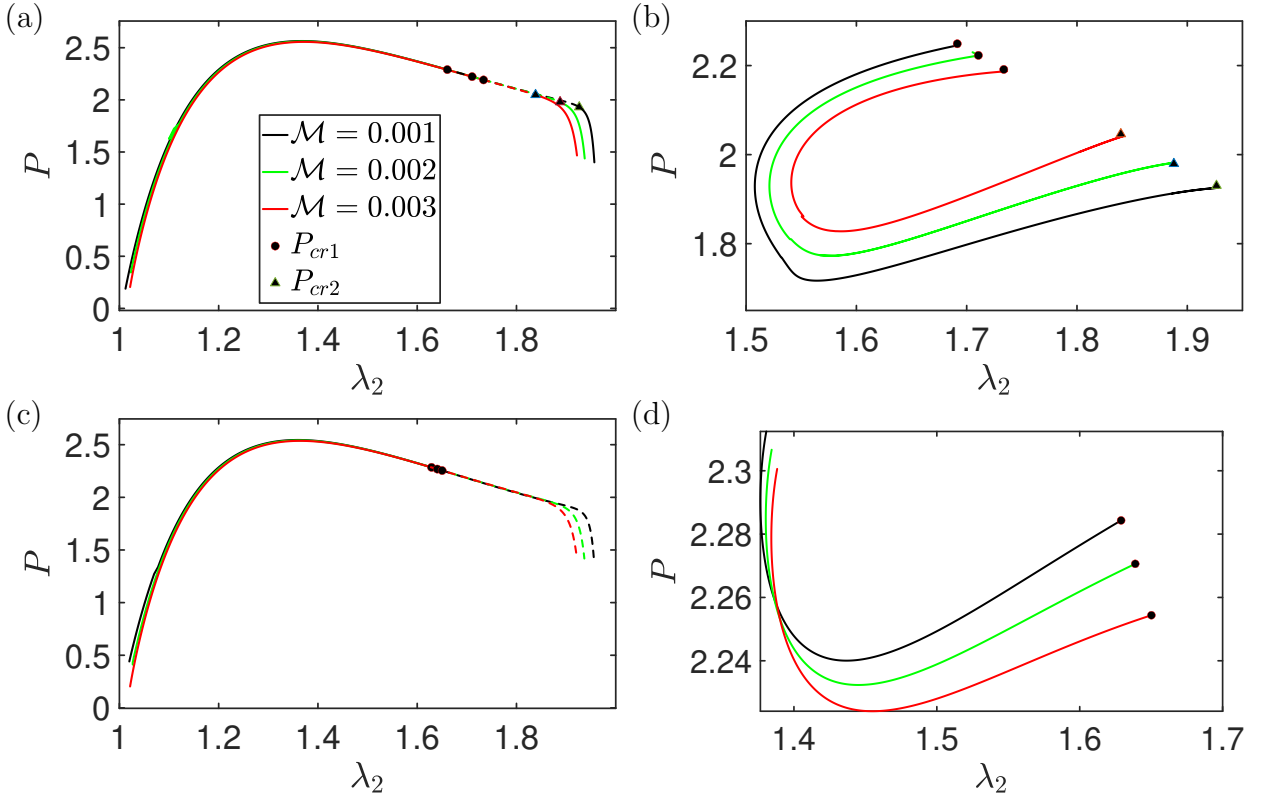


Figure 4: P vs λ_2 at equator $\theta = \pi/2$ (a) SPOM1 plane of symmetry curve. (b) SPOM1 pear-shaped curve. (c) TPOM1 plane of symmetry curve. (d) TPOM1 pear-shaped curve. The solid line represents a stable equilibrium and the dotted line represents unstable equilibrium.

symmetric solutions for a given stretch at the pole.

In Figs. 3(a) and 3(b), for the SPOM parameters, the first critical pressure, P_{cr1} (filled circle), decreases with increasing magnetic field intensity, while the second critical pressure, P_{cr2} (filled triangle), increases. Similar results are observed for the FPOM parameters (not shown in figures). Though isolated pear-shaped solutions are observed with the magnetic field in Fig. 3(b), part of the solution curve on the isolated loop is marked with dashed lines representing instability. This was not observed in the absence of magnetic field as entire isolated curve in Fig. 2(a) is found to be stable. The detailed discussion on stability can be found in the later sections.

In the case of TPOM parameters, there is only a single critical pressure where bifurcation occurs, and this bifurcation happens at progressively lower pressures as the magnetic field

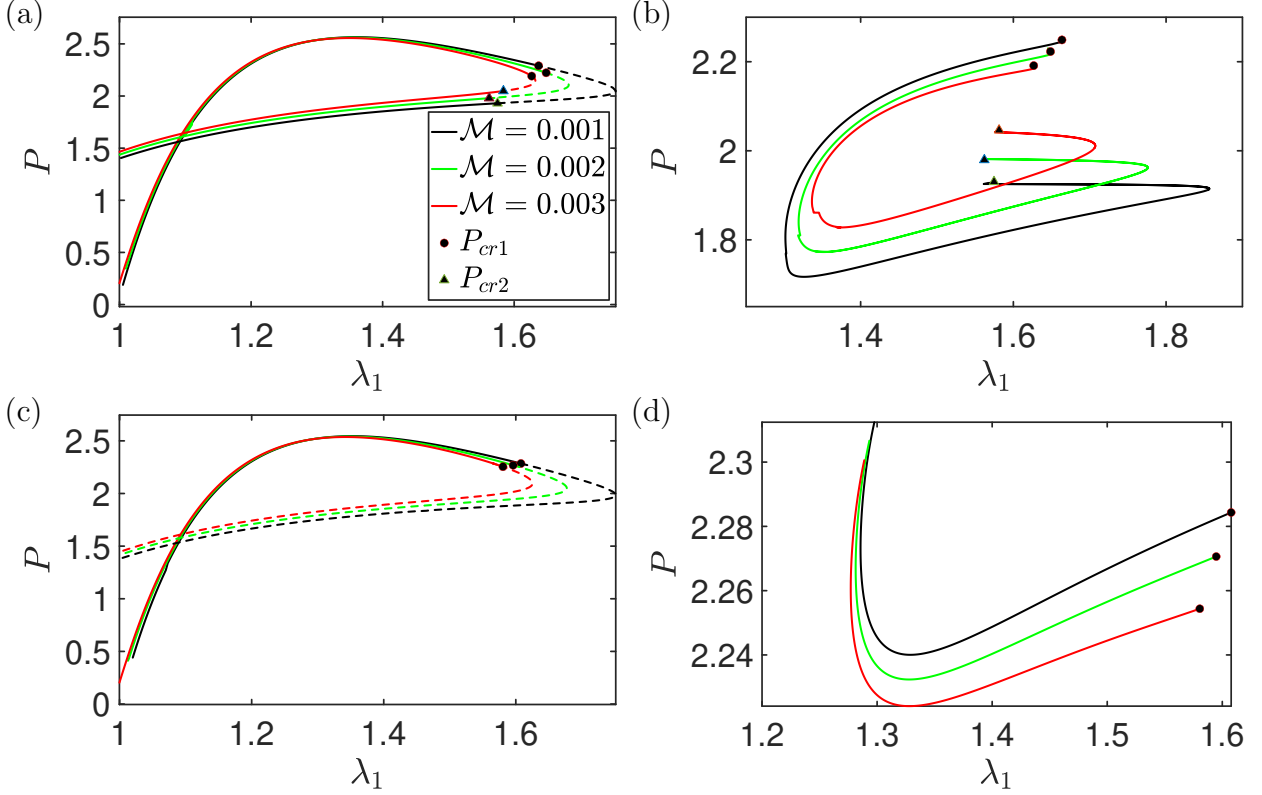


Figure 5: P vs λ_1 at equator $\theta = \pi/2$ (a) SPOM1 plane of symmetry curve. (b) SPOM1 pear-shaped curve. (c) TPOM1 plane of symmetry curve. (d) TPOM1 pear-shaped curve. The solid line represents a stable equilibrium and the dotted line represents unstable equilibrium.

strength increases, as shown in Fig. 3(c). This behavior mirrors the effect of increasing α_1 , as discussed in Section 8.1. Beyond a critical magnetic field intensity ($\mathcal{M} = 0.004$ for the SPOM model and $\mathcal{M} = 0.0078$ for the TPOM model), the bifurcated curve no longer exists (not shown in figure), and the plane of the symmetry curve remains entirely stable. It is interesting to observe that in the presence of magnetic field, the pear-shaped curve has a limit point on the pressure stretch curve which is different from the bifurcation point.

Figs. 4 and 5 show P versus λ_2 and λ_1 , respectively, at the equator for both axisymmetric and plane of symmetry breaking cases. After the turning point λ_2 at the equator nearly remains constant, as shown in Fig. 4. However, λ_1 at the equator continues to reduce after the turning point as shown in Fig. 5. When λ_1 at the equator drops below one, this corresponds to the region where the stress σ_θ becomes negative, which indicates an impending wrinkling

condition. Under the influence of a magnetic field, wrinkled configurations may appear at lower pressures along the axisymmetric branch, following the second critical point (P_{cr2}), and at the magnetic limit point.

8.3. Effect of magnetic field on balloon inflation: two coil arrangement

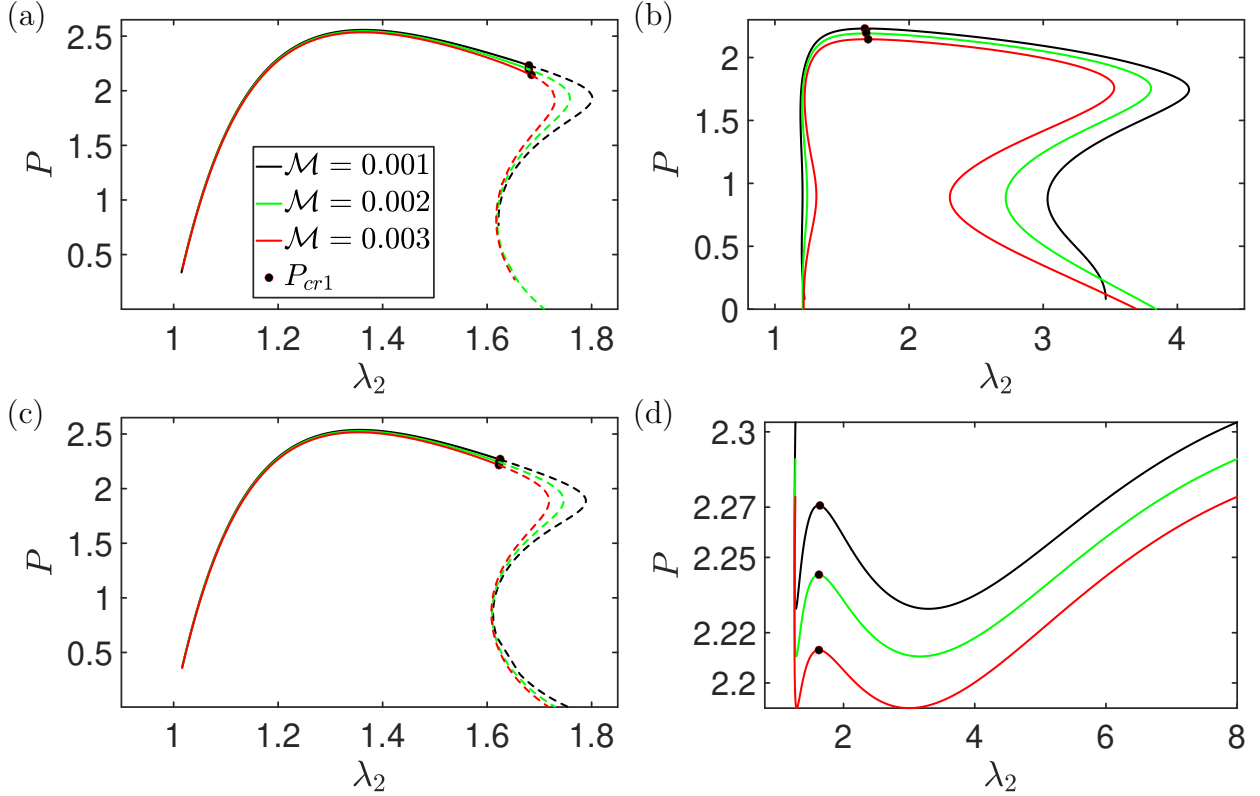


Figure 6: P vs λ_2 at pole $\theta = 0$ for two coil arrangement (a) SPOM1 plane of symmetry curve. (b) SPOM1 pear-shaped curve. (c) TPOM1 plane of symmetry curve. (d) TPOM1 pear-shaped curve. The solid line represents a stable equilibrium and the dotted line represents unstable equilibrium.

This section examines the effects of a non-uniform magnetic field generated by two coils positioned at heights $h = 1$ and $h = -1$ relative to the equator of the undeformed balloon, each with a radius $a = 1.7321$. The coil at $h = 1$ carries a counterclockwise current, while the coil at $h = -1$ carries a clockwise current. The observations for this configuration are consistent with those in Section 8.2: increasing the magnetic field intensity reduces the limit point pressure of the primary (plane of symmetry) curve, the turning point shifts to smaller

stretches with increasing field intensity, and the smallest pressure in the pre-limit point section, known as the “magnetic limit point,” marks the critical threshold for equilibrium at lowest pressure, as shown in Fig. 6(a).

Unlike the single coil arrangement, the SPOM1 material model exhibits single bifurcation point for the two coil arrangement, as illustrated in Fig. 7(b). The critical pressure at which pear-shaped bifurcation occurs decreases as the magnetic field strength increases, as shown in Fig. 7(b). The pressure vs. stretch curves for the primary and pear-shaped bifurcations in the TPOM1 model for the two-coil arrangement are similar to those observed in the single coil arrangement, as presented in Fig. 7.

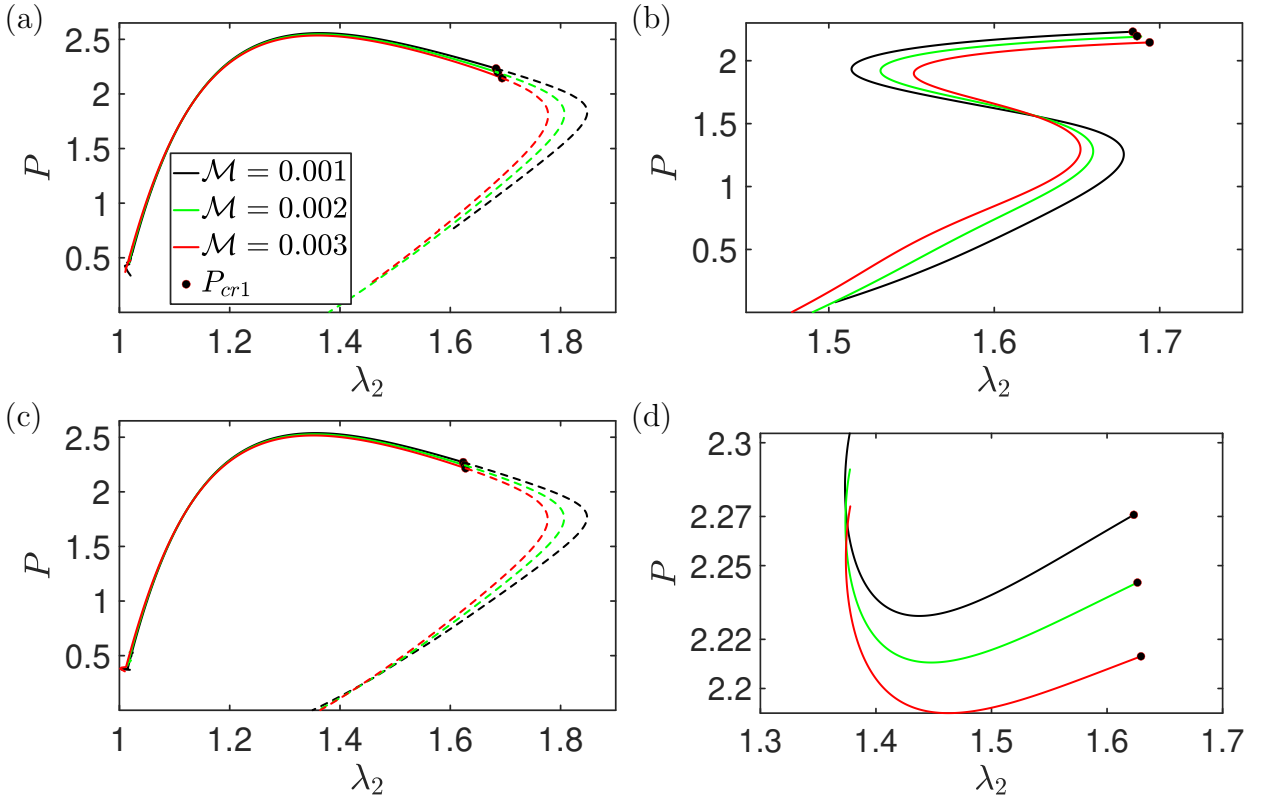


Figure 7: P vs λ_2 at equator $\theta = \pi/2$ for two coil arrangement (a) SPOM1 plane of symmetry curve. (b) SPOM1 pear shaped curve. (c) TPOM1 plane of symmetry curve. (d) TPOM1 pear shaped curve. The solid line represents a stable equilibrium and the dotted line represents unstable equilibrium.

Figs. 7 and 8 show P versus λ_2 and λ_1 , respectively, at the equator for both axisymmetric and plane of symmetry breaking cases for two coil arrangement.

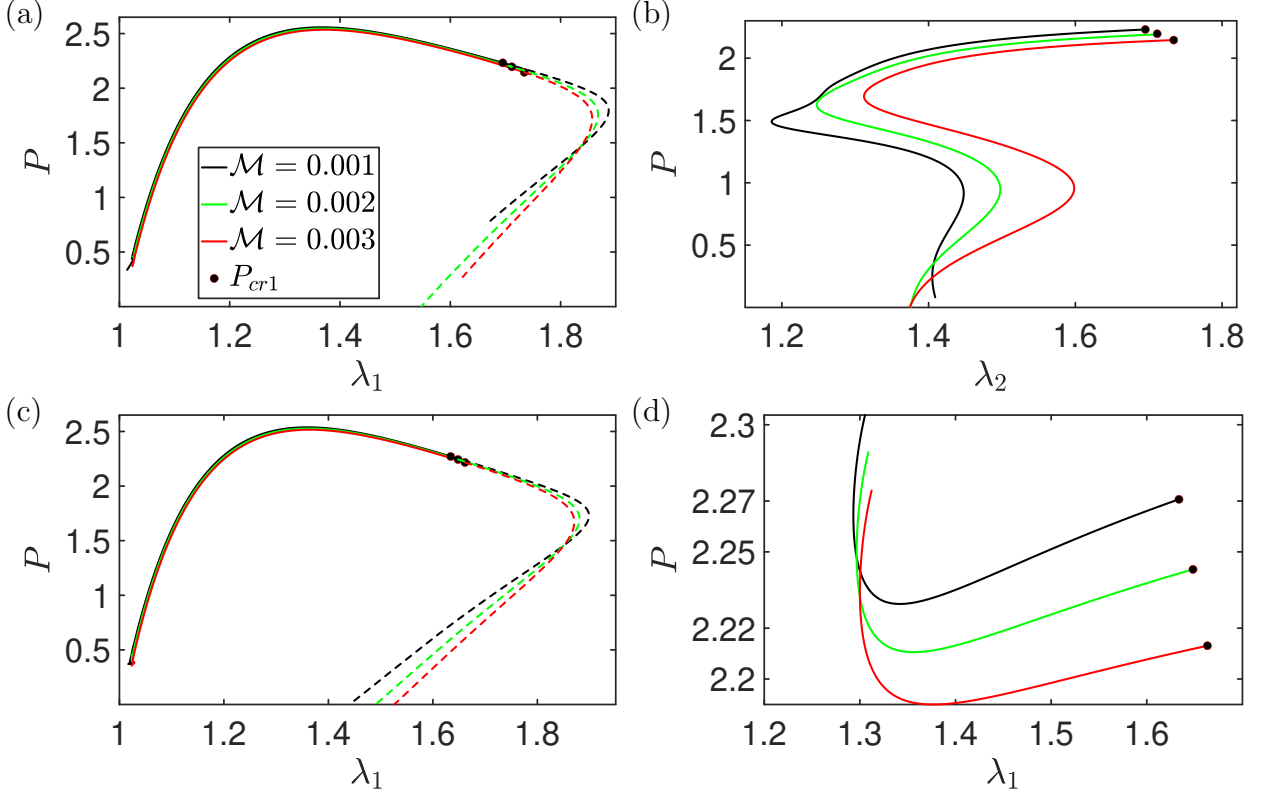


Figure 8: P vs λ_1 at equator $\theta = \pi/2$ for two coil arrangement (a) SPOM1 plane of symmetry curve. (b) SPOM1 pear-shaped curve. (c) TPOM1 plane of symmetry curve. (d) TPOM1 pear-shaped curve. The solid line represents a stable equilibrium and the dotted line represents unstable equilibrium.

8.4. Deformed Configuration

Fig. 9(a) shows the equilibrium configurations on pressure stretch curve 1 : (axisymmetric before turning point), 2 : (pear-shaped), 3 : (axisymmetric after turning point). Fig. 9(b) illustrates the deformed shapes for equilibrium configurations 1, 2 and 3. The deformed shape along the axisymmetric curve (depicted by equilibrium configuration 1) maintains axis symmetry and symmetry across the $Y^1 - Y^2$ plane. In contrast, the deformed shape along the plane-symmetry-breaking curve retains axis symmetry but lacks symmetry across the $Y^1 - Y^2$ plane (depicted by equilibrium configuration 2) and resembles a top-heavy pear shape. For the shape after the turning point (depicted by equilibrium configuration 3), a sharp change in the balloon's curvature occurs near the equator ($\theta = \pi/2$) as shown in Fig. 12(b). This sharp change is caused by two factors: (1) the membrane near the

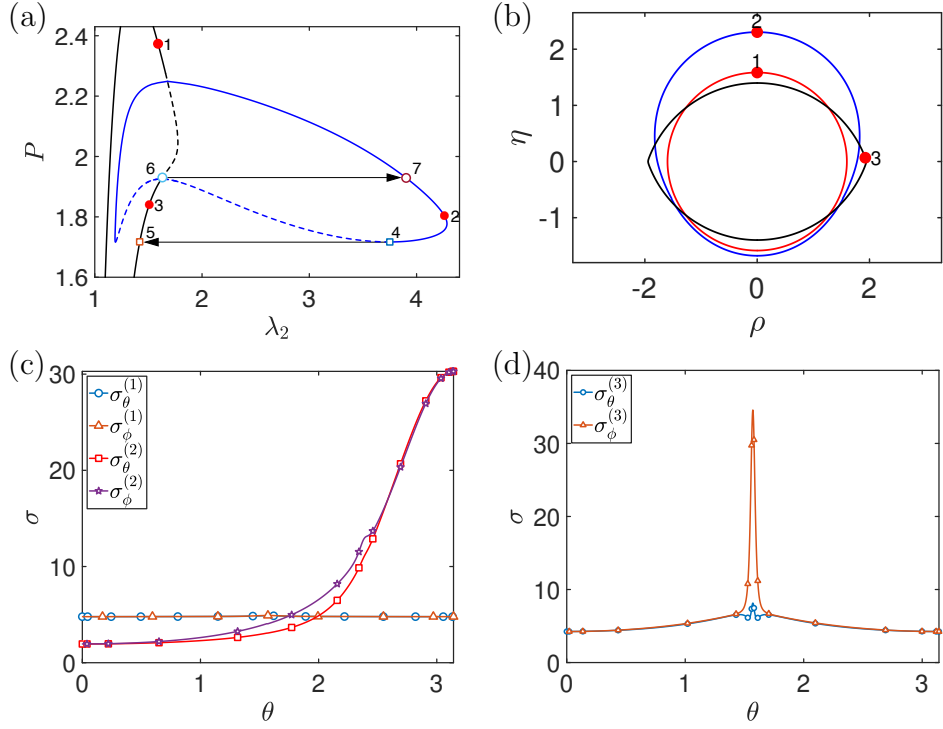


Figure 9: (a) P vs λ_2 equilibrium curves for SPOM1 model and equilibrium configurations (b) shapes of equilibrium configurations 1 (axisymmetric) 2 (pear-shaped) 3 (axisymmetric after turning point) (c) Stresses σ_θ and σ_ϕ vs θ for the configuration 1 and 2. (d) Stresses σ_θ and σ_ϕ vs θ for the configuration 3.

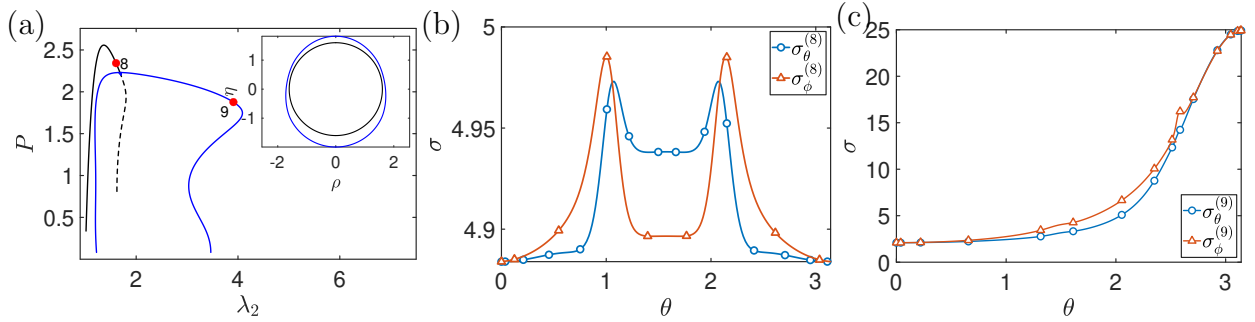


Figure 10: (a) P vs λ_2 equilibrium curves with a two coil arrangement for SPOM1 model and shapes for configurations 8 and 9. (b) Stresses σ_θ and σ_ϕ vs θ for the configuration 8. (c) Stresses σ_θ and σ_ϕ vs θ for the configuration 9.

equator is positioned very close to the current-carrying coil, resulting in a stronger magnetic field; and (2) there is a sharp variation in the radial component of the applied magnetic field around $\theta = \pi/2$. This abrupt curvature change near the equator is also reflected in the stress vs. θ plots in Fig. 9(d), where the stress component σ_ϕ shows a pronounced increase near

the theta value where membrane comes very close to current carrying coil. For equilibrium points 1 and 2, change of curvature with respect to θ is shown in Fig. 12(a).

Figure 10(a) shows the deformed shapes of the axisymmetric equilibrium configuration 8 and the pear-shaped equilibrium configuration 9 for the two-coil arrangement. The stresses, σ_θ and σ_ϕ for configurations 8 and 9, are shown in Fig. 10(b) and 10(c), respectively. The applied magnetic field and curvature for configurations 8 and 9 are presented in Fig. 11(c) and Fig. 12(c), respectively.

Equilibrium configurations for pressures below point 9 in Fig. 10(a) exhibit sharp changes in curvature, similar to configuration 3 in Fig. 9(b). This phenomenon occurs as the balloon membrane approaches very close to the two coils located at heights $h = 1$ and $h = -1$, where sharp variations in the radial component of the magnetic field are present. Consequently, the membrane experiences substantial stress concentrations, orders of magnitude higher than the ultimate tensile strength reported of magnetoelastic polymers or soft biological membranes (Raz et al. (2019); Heidarian and Kouzani (2023); Liao et al. (2023)).

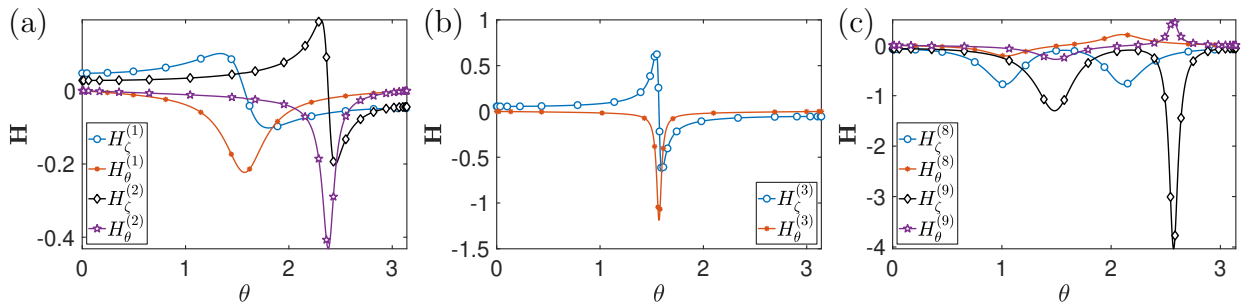


Figure 11: Applied magnetic field components H_c and H_θ vs θ on the deformed membrane. (a) Configuration 1 and 2 shown in Fig. 9(a), (b) Configuration 3, shown in Fig. 9(a). (c) Configurations 8 and 9, shown in Fig. 10(a).

8.5. Stability

Chen and Healey (1991) demonstrated the existence of an isola bifurcation in pressurized spherical membranes, forming a closed loop of non-spherical solutions during inflation. They observed that when pear-shaped and spherical configurations coexist, the pear-shaped configuration exhibits lower strain energy. Furthermore, the spherical solution branch un-

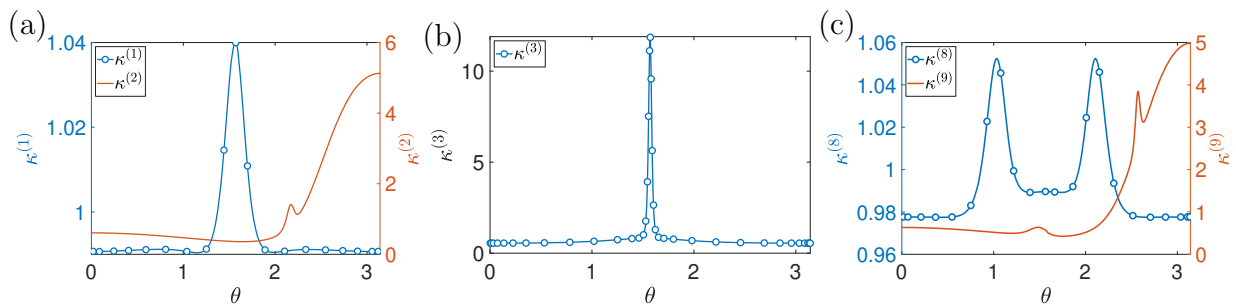


Figure 12: Gaussian curvature κ vs θ (a) for configuration 1 and 2 shown in Fig. 9(a). (b) for configuration 3 shown in Fig. 9(a). (c) for configuration 8 and 9 shown in Fig. 10(a).

dergoes symmetry-breaking via supercritical pitchfork bifurcation and reconnects to the symmetric branch through reverse supercritical pitchfork bifurcation, thereby forming the isola bifurcation.

In this work, a supercritical pitchfork bifurcation occurs during the transition from a stable axisymmetric ellipsoidal configuration to a stable pear-shaped configuration. The isolated pear-shaped bifurcation curve, representing a closed loop of symmetry-breaking solutions, reconnects to the symmetry-preserving ellipsoidal shape curve through a reverse subcritical pitchfork bifurcation. Due to the subcritical nature of bifurcation, where higher order non-linearity play an important role, part of the pear-shaped solutions is found to be unstable.

In the absence of magnetic field, isola bifurcation is observed in the SPOM model but is absent in the TPOM model, as shown in Fig. 2. When magnetic field is applied using a single coil, the closed loop of the isolated pear-shaped curve in the SPOM model shrinks toward its center (Fig. 3(b)) and eventually disappears at a critical magnetic field strength (not shown), similar to the behavior of isola bifurcation in the non-magnetic case. In the TPOM model (Fig. 3(d)), as the magnetic field increases, bifurcation occurs at progressively lower pressures and ultimately vanishes at a critical magnetic field strength (not shown).

Interestingly, when the magnetic field is applied using two coils, the isolated loop of pear-shaped solutions is absent in both the SPOM and TPOM models, as shown in Fig. 6. However, with a single coil, the isolated loop of pear-shaped solutions appears but only persists below a certain critical magnetic field strength.

As previously mentioned, stable pear-shaped and unstable axisymmetric configurations are possible only when the Hessian matrix in 46 is not positive definite, i.e., at least one of the eigenvalues of the matrix must cross zero and become negative. Let $\mathbf{v} = \Lambda \mathbf{u}$ represent a perturbation vector, where \mathbf{u} is the unit eigenvector associated with the negative eigenvalue of the Hessian matrix and Λ is the unknown (small) magnitude of the perturbation vector. Determining Λ will fully characterize the pear-shaped configuration. The perturbed potential energy can then be expressed as,

$$\tilde{E}(\Lambda) = E + \Lambda E_1 + \Lambda^2 E_2 + \Lambda^3 E_3 + \Lambda^4 E_4 + O(\Lambda^5). \quad (47)$$

For equilibrium, we must have,

$$\frac{\partial \tilde{E}}{\partial \Lambda} = 0. \quad (48)$$

Solution of 48 gives the value of Λ .

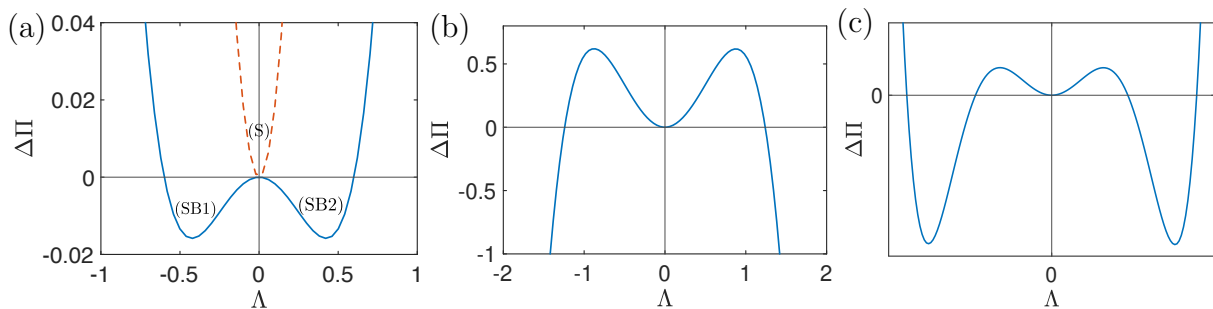


Figure 13: (a) Potential energy difference $\Delta\Pi$ vs Λ showing axisymmetric equilibrium (S) and symmetry breaking configurations (SB1) and (SB2) near pressure P_{cr1} for $\mathcal{M} = 1 \times 10^{-3}$. (b) $\Delta\Pi$ vs Λ at P_{cr2} for $\mathcal{M} = 1 \times 10^{-3}$. (c) Qualitative potential energy difference $\Delta\Pi$ vs Λ for reverse subcritical pitchfork bifurcation.

To visualize the potential energy for SPOM1 model and $\mathcal{M} = 1 \times 10^{-3}$ near the critical pressure points (P_{cr1} and P_{cr2}), where the closed loop of the isolated pear-shaped solutions starts and merges, we plot the potential difference $\Delta E = (\tilde{E} - E)$ against Λ in Fig. 13.

In Fig. 13(a), the energy plot corresponds to configuration S, just above pressure value P_{cr1} . At this point, $\Lambda = 0$ corresponds to the axisymmetric solution, which is the only stable configuration. However, just below P_{cr1} , a supercritical pitchfork bifurcation occurs, giving

rise to two stable pear-shaped configurations, corresponding to $\Lambda = 0.4208$ and $\Lambda = -0.4208$ denoted as SB1 and SB2.

Fig. 13(b) illustrates the energy landscape just below P_{cr2} , where a reverse subcritical pitchfork bifurcation occurs. At this point, the axisymmetric configuration remains stable, while two unstable pear-shaped configurations, corresponding to $\Lambda = 0.87723$ and $\Lambda = -0.87723$, bifurcate from it. However, Fig. 13(b) provides only a partial representation of the reverse subcritical pitchfork bifurcation, as the energy expansion is considered only up to the Λ^4 term in (47), revealing only two unstable solutions and one stable solution. A complete qualitative depiction of the energy landscape for the reverse subcritical pitchfork bifurcation is presented in Fig. 13(c).

Fig. 9(a) shows the axisymmetric and pear-shaped equilibrium P vs λ_2 curves at the poles ($\theta = 0/\pi$) for the SPOM1 model with $\mathcal{M} = 1 \times 10^{-3}$. These curves illustrate the snap-through transition from the pear-shaped configuration 4 to the axisymmetric configuration 5, and from an axisymmetric configuration 6 to a pear-shaped configuration 7.

If we consider pressure as the control parameter for a balloon under the influence of a magnetic field with intensity $\mathcal{M} = 1 \times 10^{-3}$, the system initially reaches the pear-shaped configuration 4. However, if the pressure is reduced even slightly further, the equilibrium configuration abruptly snaps through from the pear-shaped configuration to the axisymmetric configuration 5. This snap-through behavior occurs because the pear-shaped equilibrium curve (blue curve in Fig. 9(a)) becomes unstable for pressures below the equilibrium configuration point 4. From axisymmetric configuration 5 if we increase the pressure even very slightly the equilibrium configuration abruptly snaps through from the axisymmetric configuration to the pear-shaped configuration 6.

The stability of the plane of symmetry-preserving and pear-shaped equilibrium configurations was examined by introducing small asymmetric perturbations around the determined equilibrium solutions. However, no asymmetric bifurcation was observed and both configurations were found to remain stable under small asymmetric perturbations.

9. Conclusion

Axisymmetric inflation of an initially spherical magnetoelastic balloon is studied, focusing on stability under both non-magnetic and magnetic conditions. Stability was analyzed using axisymmetric and asymmetric perturbations represented by Legendre's polynomials of $\cos\theta$. In the presence of a magnetic field generated by a single coil, the axisymmetric curve bifurcates into a pear-shaped configuration through a supercritical pitchfork bifurcation, forming an isolated bifurcation loop of pear-shaped solutions similar to the non-magnetic case. However, unlike the non-magnetic scenario where the isola curve rejoins via a reverse supercritical bifurcation, isolated bifurcation loop of pear-shaped solutions rejoins through a reverse subcritical pitchfork bifurcation in the magnetic case. As the magnetic field intensity increases, the isolated bifurcation loop of pear-shaped solutions shrinks and eventually disappears at a critical field value, mirroring the effect of increasing the material parameter α_1 in the non-magnetic case. For a magnetic field generated by two coils, the isolated bifurcation loop of pear-shaped solutions is absent for SPOM and FPOM models, though the pressure at which pear-shaped bifurcations occur decreases with increasing magnetic field intensity. These findings demonstrate that both the applied magnetic field and material parameters strongly influence the stability of axisymmetric configurations in magnetoelastic balloons. Additionally, snap-through phenomena between axisymmetric and pear-shaped configurations are observed under the influence of the magnetic field.

In the present analysis, asymmetric perturbations have been considered for both symmetry-preserving and pear-shaped solutions. However, since the perturbations introduced were small, this linear perturbation approach can only capture asymmetric solutions that are very close to axisymmetric ones. As a result, no asymmetric solutions were identified for either the magnetic or non-magnetic cases. Extending the analysis to include more general perturbations would be valuable for determining such solutions.

Coupling the magnetoelastic inflation of a balloon with solvent diffusion gives rise to the problem of magnetic gel balloon inflation. Investigating the stability of such a multiphysics system involving magnetism, diffusion, and deformation interactions presents an intriguing

challenge for future work.

Acknowledgement

S.N.K. and G.T. acknowledge the Ministry of Education (MoE), Government of India, for providing research support. We also thank Arun Krishna B.J. for the helpful discussions.

Appendix A.

The total potential energy for inflation of a magneto-elastic balloon under the application of a magnetic field is given by (25)) as,

$$E_T = \int_0^{2\pi} \int_0^\pi \left[\left(\Phi - \frac{1}{2} \mu_o \chi \mathcal{M} \mathcal{H}^2 \right) \sin \theta + \frac{1}{2} P \lambda_2^2 \sin^2 \theta \eta_{,\theta} \right] d\theta d\phi, \quad (\text{A.1})$$

$$E_T = \int_0^{2\pi} \int_0^\pi \Pi d\theta d\phi,$$

From the principle of minimum potential energy, the equilibrium equations in terms of λ_2 and η are $\delta_{\lambda_\theta} \hat{\Pi} = 0$ and $\delta_\eta \hat{\Pi} = 0$ are given as follows,

Appendix A.1. Governing equations

$$\frac{\partial \Pi}{\partial \lambda_2} - \frac{d}{d\theta} \left(\frac{\partial \Pi}{\partial \lambda_{2,\theta}} \right) = 0, \quad \frac{\partial \Pi}{\partial \eta} - \frac{d}{d\theta} \frac{\partial \Pi}{\partial \eta_{,\theta}} = 0. \quad (\text{A.2})$$

Using the substitution $v = \lambda_{2,\theta} \sin \theta$ and $\eta_{,\theta} = w$, (A.2)₁ can be further expressed as

$$\frac{d}{d\theta} [\Phi_{,v} \sin^2 \theta] = \Phi_{,\lambda_2} \sin \theta - \mu_o \chi \mathcal{M} \mathcal{H} \mathcal{H}_{,\lambda_2} \sin \theta + P \lambda_2 w \sin^2 \theta$$

Expanding the above equation further with $(\cdot)_{,z} = \frac{\partial(\cdot)}{\partial z}$

$$\begin{aligned} \sin^2 \theta \left[\Phi_{,vv} v_{,\theta} + \Phi_{,vw} w_{,\theta} + \Phi_{,v\lambda_2} \frac{v}{\sin \theta} + \Phi_{,v \cos \theta} \sin \theta \right] &= \Phi_{,\lambda_2} \sin \theta - \mu_o \chi \mathcal{M} \mathcal{H} \mathcal{H}_{,\lambda_2} \sin \theta \\ &+ P \lambda_2 w \sin^2 \theta - 2 \sin \theta \cos \theta \Phi_{,v} \end{aligned}$$

$$\Phi_{,vv} v_{,\theta} + \Phi_{,vw} w_{,\theta} = \frac{\Phi_{,\lambda_2} - 2 \cos \theta \Phi_{,v}}{\sin \theta} - \Phi_{,v\lambda_2} \frac{v}{\sin \theta} - \mu_o \chi \mathcal{M} \mathcal{H} \mathcal{H}_{,\lambda_2} \frac{1}{\sin \theta} + P \lambda_2 w - \Phi_{,v \cos \theta} \sin \theta \quad (\text{A.3})$$

The first and second terms on the right-hand side of the equation (A.3) are of form $\frac{0}{0}$ at poles of the balloon, i.e. at $\theta = 0$ and $\theta = \pi$ due to division by $\sin \theta$. These terms at poles are calculated using L'Hôpital's rule. In the third term $\sin \theta$ in denominator gets cancelled by $\sin \theta$ term in the numerator of the term $\frac{\partial \mathcal{H}}{\partial \lambda_2}$. The presence of a mathematical form $\frac{0}{0}$ which is resolved using L'Hôpital's rule is called the removable singularity.

Similarly, (A.2)₂ can be expressed as

$$\frac{d}{d\theta} \left[\Phi_{,w} \sin \theta + \frac{1}{2} P \lambda_2^2 \sin^2 \theta \right] = -\mu_0 \chi \mathcal{M} \mathcal{H} \mathcal{H}_{,\eta} \sin \theta$$

$$\frac{d\Phi_{,w}}{d\theta} = -\mu_0 \chi \mathcal{M} \mathcal{H} \mathcal{H}_{,\eta} - \cot \theta \Phi_{,w} - P \lambda_2 v - P \cos \theta \lambda_2^2$$

$$\Phi_{,wv} v_{,\theta} + \Phi_{,ww} w_{,\theta} = -\mu_0 \chi \mathcal{M} \mathcal{H} \mathcal{H}_{,\eta} - \Phi_{,w\lambda_2} \frac{v}{\sin \theta} - \cot \theta \Phi_{,w} - P \lambda_2 v - P \lambda_2^2 \cos \theta - \Phi_{,w \cos \theta} \sin \theta \quad (\text{A.4})$$

Similar to the removable singularity case discussed in the section (Appendix A.1) the second and third terms on the right-hand side of the equation (A.4) are of form $\frac{0}{0}$ at poles of the balloon, i.e. at $\theta = 0$ and $\theta = \pi$ due to division by $\sin \theta$. These terms at poles are calculated using L'Hôpital's rule.

Appendix A.2. Applied magnetic field

It is convenient to express the applied magnetic field \mathbf{h}_a in both coordinate systems i.e. Cartesian as well as curvilinear coordinate systems associated with deformed configuration. From equations (1), (3) tangent vectors i.e. bases for curvilinear coordinates (θ, ϕ, ζ) , can be written in terms of bases vectors of Cartesian coordinate system as,

$$\hat{\mathbf{g}}_i = Q_{ij} \hat{\mathbf{e}}_j \quad (\text{A.5})$$

$$\text{where } Q_{11} = \frac{\rho_{,\theta} \cos \phi}{\sqrt{\rho_{,\theta}^2 + \eta_{,\theta}^2}}, \quad Q_{12} = -\sin \phi,$$

$$Q_{21} = -\sin \phi, \quad Q_{22} = \cos \phi, \quad Q_{23} = 0, \quad Q_{31} = -\frac{\eta_{,\theta} \cos \phi}{\sqrt{\rho_{,\theta}^2 + \eta_{,\theta}^2}}, \quad (\text{A.6})$$

$$Q_{32} = -\frac{\eta_{,\theta} \sin \phi}{\sqrt{\rho_{,\theta}^2 + \eta_{,\theta}^2}}, \quad Q_{33} = -\frac{\rho_{,\theta}}{\sqrt{\rho_{,\theta}^2 + \eta_{,\theta}^2}},$$

here $\hat{\mathbf{g}}_3 = \mathbf{n}$ the outward surface normal as mentioned in (4). Inverting equation (A.5), Cartesian bases can be written in terms of curvilinear bases as follows,

$$\hat{\mathbf{e}}_i = \bar{Q}_{ij} \hat{\mathbf{g}}_j, \quad (\text{A.7})$$

where $\bar{Q}_{ij} = Q_{ij}^{-1} = Q_{ji}$. Using equations (A.7), (A.5) and (16) the applied magnetic field \mathbf{h}_a can be written in the curvilinear bases associated with deformed configuration as follows,

$$\begin{aligned} \mathbf{h}_a = & \frac{I}{4\pi R_0} \int_0^{2\pi} \hat{\mathbf{g}}_1 \frac{\eta_{,\theta} a^2 + (\rho_{,\theta} (\eta - h) a - \rho \eta_{,\theta} a) \cos(\phi_i - \phi)}{\left(\sqrt{\rho_{,\theta}^2 + \eta_{,\theta}^2}\right) (\rho^2 + (\eta - h)^2 + a^2 - 2\rho a \cos(\phi_i - \phi))^{3/2}} d\phi_i \\ & + \frac{I}{4\pi R_0} \int_0^{2\pi} \hat{\mathbf{g}}_3 \frac{\rho_{,\theta} a^2 - (\eta_{,\theta} (\eta - h) a + \rho_{,\theta} \rho a) \cos(\phi_i - \phi)}{\left(\sqrt{\rho_{,\theta}^2 + \eta_{,\theta}^2}\right) (\rho^2 + (\eta - h)^2 + a^2 - 2\rho a \cos(\phi_i - \phi))^{3/2}} d\phi_i \end{aligned} \quad (\text{A.8})$$

Expressions for the applied magnetic field \mathbf{h}_a given in equations (16) and (A.8) can be written shortly as,

$$\begin{aligned} \mathbf{h}_a = & \frac{I}{4\pi R_0} (\hat{\mathbf{e}}_1(h_a)_1 + \hat{\mathbf{e}}_2(h_a)_2 + \hat{\mathbf{e}}_3(h_a)_3) \\ = & \frac{I}{4\pi R_0} (\hat{\mathbf{g}}_1(h_a)_\theta + \hat{\mathbf{g}}_3(h_a)_\zeta) \end{aligned} \quad (\text{A.9})$$

References

- M. Barham, D. J. Steigmann, M. McElfresh, and R. E. Rudd. 2007. Finite deformation of a pressurized magnetoelastic membrane in a stationary dipole field. *Acta Mech.*, 191(1):1–19.
- M. Barham, D. J. Steigmann, M. McElfresh, and R. E. Rudd. 2008. Limit-point instability of a magnetoelastic membrane in a stationary magnetic field. *Smart Mater. Struct.*, 17(5):055003.
- N. W. Bartlett, M. T. Tolley, J. T. B. Overvelde, J. C. Weaver, B. Mosadegh, K. Bertoldi, G. M. Whitesides, and R. J. Wood. 2015. A 3d-printed, functionally graded soft robot powered by combustion. *Science*, 349(6244):161–165.
- L. Bauer, E. L. Reiss, and H. B. Keller. 1970. Axisymmetric buckling of hollow spheres and hemispheres. *Comm. Pure Appl. Math.*, 23(4):529–568.
- Y.-C. Chen and T. J. Healey. 1991. Bifurcation to pear-shaped equilibria of pressurized spherical membranes. *Int. J. Non-Linear Mech.*, 26(3):279–291.
- J. Cheng, Z. Jia, H. Guo, Z. Nie, and T. Li. 2019. Delayed burst of a gel balloon. *J. Mech. Phys. Solids*, 124:143–158.

- D. Dellwo, H. B. Keller, B. J. Matkowsky, and E. L. Reiss. 1982. On the birth of isolas. *SIAM J. Appl. Math.*, 42(5):956–963.
- Y. Fu and Y. Xie. 2014. Stability of pear-shaped configurations bifurcated from a pressurized spherical balloon. *J. Mech. Phys. Solids*, 68:33–44.
- A. Ghosh and S. Basu. 2021. Soft dielectric elastomer tubes in an electric field. *J. Mech. Phys. Solids*, 150:104371.
- P. Heidarian and A. Z. Kouzani. 2023. Starch-g-acrylic acid/magnetic nanochitin self-healing ferrogels as flexible soft strain sensors. *Sens.*, 23(3):1138.
- J. Humphrey. 2003. Review paper: Continuum biomechanics of soft biological tissues. *Proc. R. Soc. A*, 459(2029):3–46.
- C. Jenkins. 01 2001. Gossamer spacecraft: Membrane and inflatable structures technology for space applications. *AIAA*.
- H. B. Keller and A. W. Wolfe. 1965. On the nonunique equilibrium states and buckling mechanism of spherical shells. *J. Soc. Ind. Appl. Math.*, 13(3):674–705.
- A. D. Kerr and L. El-Bayoumy. *Equilibrium and stability of a shallow arch subjected to a uniform lateral load*. Q. Appl. Math., 1968.
- D.-H. Kim, N. Lu, R. Ghaffari, Y.-S. Kim, S. P. Lee, L. Xu, J. Wu, R.-H. Kim, J. Song, Z. Liu, J. Viventi, B. de Graff, B. Elolampi, M. Mansour, M. J. Slepian, S. Hwang, J. D. Moss, S.-M. Won, Y. Huang, B. Litt, and J. A. Rogers. 2011. Materials for multifunctional balloon catheters with capabilities in cardiac electrophysiological mapping and ablation therapy. *Nat. Mater.*, 10(4):316–323.
- X. Liang and S. Cai. 2015. Shape Bifurcation of a Spherical Dielectric Elastomer Balloon Under the Actions of Internal Pressure and Electric Voltage. *J. Appl. Mech.*, 82(10):101002.
- Z. Liao, O. Zoumhani, and C. M. Boutry. 2023. Recent advances in magnetic polymer composites for biomems: A review. *Mater.*, 16(10):3802.
- J. A. Nelder and R. Mead. 1965. A simplex method for function minimization. *Comput. J.*, 7(4):308–313.
- A. Patil, A. Nordmark, and A. Eriksson. 2015. Instability investigation on fluid-loaded pre-stretched cylindrical membranes. *Proc. R. Soc. A*, 471(2177):20150016.
- A. Patil, A. Nordmark, and A. Eriksson. 2016. Instabilities of wrinkled membranes with pressure loadings. *J. Mech. Phys. Solids*, 94:298–315.
- P. Raz, T. Brosh, G. Ronen, and H. Tal. 2019. Tensile properties of three selected collagen membranes. *Biomed Res. Int.*, 2019(1):5163603.
- N. H. Reddy and P. Saxena. 2017. Limit points in the free inflation of a magnetoelastic toroidal membrane. *Int. J. Non-Linear Mech.*, 95:248–263.
- N. H. Reddy and P. Saxena. 2018. Instabilities in the axisymmetric magnetoelastic deformation of a

- cylindrical membrane. *Int. J. Solids Struct.*, 136-137:203–219.
- S. Roychowdhury and A. DasGupta. 2015a. Inflating a flat toroidal membrane. *Int. J. Solids Struct.*, 67:182–191.
- S. Roychowdhury and A. DasGupta. 2015b. On the response and stability of an inflated toroidal membrane under radial loading. *Int. J. Non-Linear Mech.*, 77:254–264.
- S. Roychowdhury and A. DasGupta. 2018. Symmetry breaking during inflation of a toroidal membrane. *J. Mech. Phys. Solids*, 121:328–340.
- P. Saxena, N. H. Reddy, and S. P. Pradhan. 2019. Magnetoelastic deformation of a circular membrane: Wrinkling and limit point instabilities. *Int. J. Non-Linear Mech.*, 116:250–261.
- G. Tamadapu. 2022. Swelling and inflation of a toroidal gel balloon. *Int. J. Non-Linear Mech.*, 138:103838.
- G. Tamadapu and A. DasGupta. 2014a. Effect of curvature and anisotropy on the finite inflation of a hyperelastic toroidal membrane. *Euro. J. Mech. A/Solids.*, 46:106–114.
- G. Tamadapu and A. DasGupta. 2014b. Finite inflation of a hyperelastic toroidal membrane over a cylindrical rim. *Int. J. Solids Struct.*, 51(2):430–439.
- G. Tamadapu, N. N. Dhavale, and A. DasGupta. 2013. Geometrical feature of the scaling behavior of the limit-point pressure of inflated hyperelastic membranes. *Phys. Rev. E*, 88:053201.
- C. Truesdell, W. Noll, and S. Antman. 2004. The non-linear field theory of mechanics. *Handb. Phys.*, 3.
- T. Wang, F. Xu, Y. Huo, and M. Potier-Ferry. 2018. Snap-through instabilities of pressurized balloons: Pear-shaped bifurcation and localized bulging. *Int. J. Non-Linear Mech.*, 98:137–144.
- Y. Yao, M. T. McDowell, I. Ryu, H. Wu, N. Liu, L. Hu, W. D. Nix, and Y. Cui. 2011. Interconnected silicon hollow nanospheres for lithium-ion battery anodes with long cycle life. *Nano Lett.*, 11(7):2949–2954.
- J. Yi, G. Zou, J. Huang, X. Ren, Q. Tian, Q. Yu, P. Wang, Y. Yuan, W. Tang, C. Wang, L. Liang, Z. Cao, Y. Li, M. Yu, Y. Jiang, F. Zhang, X. Yang, W. Li, X. Wang, Y. Luo, X. J. Loh, G. Li, B. Hu, Z. Liu, H. Gao, and X. Chen. 2023. Water-responsive supercontractile polymer films for bioelectronic interfaces. *Nature*, 624(7991):295–302.